

Temperature Effects
on
Dynamic Fracture of Pipeline Steel

by

Sourayon Chanda

A thesis submitted in partial fulfillment of the requirements for the degree of

Master of Science

Department of Mechanical Engineering
University of Alberta

© Sourayon Chanda, 2015

Abstract

The effective layout of pipelines for mass transportation of oil/gas is a major area of research in the present world. Due to fracture of pipelines, long-lasting and catastrophic hazards may be initiated. Hence, study of dynamic fracture of pipeline steel (PS) is a major research topic in pipeline industry. In many colder parts of the world, like northern Canada, the temperature varies from about -50°C in winter to $+35^{\circ}\text{C}$ in summer. Hence a thorough knowledge of the temperature dependent performance of PS is crucial for efficient design of pipelines. The present thesis aims to address this issue by studying the effects of temperature variation on dynamic fracture characteristics of PS.

The present work aims to develop a temperature dependent cohesive zone model (CZM)-based finite element (FE) analysis to simulate drop weight tear test (DWTT) (Chanda and Ru, 2015a). The primary work of this project is to identify the key CZM parameters that are affected by temperature variations and co-relate these parameters with known mechanical properties of PS (Chanda and Ru, 2015b). Based on these correlations, a temperature dependent cohesive zone model has been presented. To achieve this goal, the true stress strain behavior of pipeline steel have been represented by a modified form of Johnson & Cook model (Johnson and Cook, 1985) and a non-linear temperature dependency of fracture toughness for PS has been employed. The FE modeling of the CZM has been done using Abaqus/CAE 6.13. The model has been

validated by comparing with the load-displacement curves from actual DWTT ([Shim et al., 2010](#)).

The FE simulations of DWTT enable us to study the dynamic fracture behavior of PS at different temperatures. In this analysis, the time history of crack propagation for six different temperatures has been plotted. The obtained relationships show a region of steady-state crack growth during which toughness parameters like crack tip opening angle (CTOA) and crack tip opening displacement (CTOD) remain almost constant. This observation corresponds to experimental findings in this area ([Kanninen et al., 1979](#), [Yuan and Brocks, 1991](#)). Further, the steady state energy from load-displacement curve seems to decrease steeply with decrease in temperature. The steady state toughness parameters like CTOA and CTOD have been obtained for each simulation. These toughness parameters were found to exhibit an increase with increase in temperature which can be formulated using an exponential relation. These results are consistent with temperature variation of experimentally determined CTOD values for steel reported in the literature ([Ebrahimi and Seo, 1996](#), [Sorem et al., 1991](#)).

In short, the present thesis reports a simple but holistic approach to analyze the fracture behavior of PS at varying temperature using a temperature dependent CZM-based FE model.

Acknowledgement

I would like to take this opportunity to heartily thank my supervisor Dr. CQ Ru for his support and motivation towards the present research. His able assistance and guidance towards this thesis made the present research what it is today. Working under him, I also learnt a lot about documenting my research and presenting to the wider scientific community.

I am also indebted to Dr. YJ Wang, a postdoctoral fellow in our group at the University of Alberta for his valuable comments and suggestions. The support of Dr. PS Yu, a past postdoctoral fellow of our group is also acknowledged.

This work was supported by NSERC (National Science and Engineering Research Council) of Canada (CRD program) and TransCanada Pipelines Ltd. and we are very grateful for their assistance.

I would like to anonymously thank all the fellow researchers and friends who have helped me directly or indirectly to continue my studies at the University of Alberta.

Last but not the least, I would like to thank my entire family for their continued moral support and motivation throughout this research.

Contents

Abstract	ii
Acknowledgement	iv
List of Abbreviations	xi
1 Introduction	1
1.1 Pipeline’s role in modern oil and gas industry	1
1.2 Historical importance of temperature dependence of fracture	3
1.3 Fracture of pipelines	3
1.4 Temperature effects on fracture of pipelines	5
1.5 Objectives of the thesis	5
2 Background on pipeline steel	7
2.1 Pipeline steel	8
2.1.1 X80 steel	9
2.2 Stress-strain curves for pipeline steel	9
2.2.1 Temperature-dependent stress-strain curves for pipeline steel . .	11
2.2.2 Relationship between ultimate stress and temperature	12
2.3 Fracture toughness	12
2.3.1 Toughness parameters	13

2.3.2	Temperature dependence of fracture toughness	14
2.4	Fracture toughness testing	15
2.4.1	Charpy impact test	15
2.4.2	DWTT	16
2.5	Cohesive zone model (CZM)	18
2.5.1	Existing CZM	18
2.5.2	Existing temperature dependent CZM	20
3	Temperature dependency of mechanical properties of pipeline steel	24
3.1	Modified Johnson-Cook strength model	24
3.1.1	Original Johnson-Cook model	25
3.1.2	Modification for low temperature applications	26
3.1.3	Modification for strain rate term	29
3.1.4	Final modified form of Johnson-Cook model	32
3.1.5	Calibration of the modified strength model	33
3.2	Maximum true stress	36
3.2.1	Relationship between ultimate stress and maximum fracture strain	37
3.3	Damage due to void formation	38
3.3.1	Temperature dependency of damage variable	41
3.4	Mathematical model for temperature dependency of fracture energy . .	42
3.4.1	Ductile to brittle transition	43
3.4.2	Upper-shelf and lower-shelf fracture energy	43
4	Temperature dependent cohesive zone model	47
4.1	Mathematical model for traction-separation law	47
4.2	Temperature effects on traction-separation law	49
4.3	Maximum traction	50

4.4	Cohesive energy and damage evolution	50
4.5	Effect of dynamic crack growth	51
5	Temperature dependent CZM-based finite element model	54
5.1	Temperature independent FE models	54
5.2	Temperature-dependent FE model	55
5.2.1	Specifications of DWTT	56
5.2.2	Meshing of the model	56
5.3	Verification of the present model	58
6	Temperature dependence of dynamic fracture of pipeline steel	62
6.1	Temperature effect on load displacement curve	62
6.2	Temperature effect on crack length and crack speed	66
6.3	Temperature effect on CTOA	68
6.4	Temperature effect on CTOD	71
6.5	Temperature dependency of toughness parameters	73
7	Summary and Future Work	76
7.1	Summary of the thesis	76
7.2	Future Work	78

List of Tables

1.1	Causes of pipeline rupture in Canada from 1992 to 2012 as reported by National Energy Board, Canada	4
2.1	Chemical composition of different grades of steel used for linepipes.	8
3.1	Variation of damage variable with temperature obtained from numerical simulations	41
3.2	Mechanical properties of X80 steel used in the FE model	42
4.1	Example of separation rate and corresponding k_d at steady-state for the FE simulation at a temperature of -30°C	52
5.1	Details of meshing for individual instances	58
6.1	Maximum load and steady state energy for the load displacement curves at different temperature	63
6.2	Average steady state CTOA and CTOD at different temperature	73
6.3	Representative values of the toughness parameters for Eq. (6.1)	74

List of Figures

2.1	Standard specimen for uniaxial tensile test with circular cross-section (William D. Callister, 2001).	10
2.2	Stress strain curve for PS for room temperature.	10
2.3	True stress strain curves at three different temperatures for X80 steel (Akselsen et al., 2012, Jung et al., 2013, Ren and Ru, 2013).	11
2.4	Curve fit of Yaroshewich-Ryvkina model relating ultimate strength and temperature for PS	13
2.5	Variation of fracture toughness with temperature (Kaminskii and Galatenko, 1999)	15
2.6	Schematic of Charpy impact test (Anderson, 2005)	16
2.7	Schematic of DWTT (ASTM Standard E 436)	17
2.8	Cohesive zone modeling near crack tip (Sun and Jin, 2012): a is crack length, x is the crack propagation direction, d is cohesive zone length. . .	19
2.9	Different forms of the traction-separation relationships used for cohesive zone modeling	23
3.1	Verification of modification of temperature term in Johnson-Cook model	30
3.2	Verification of modification of strain rate term in Johnson-Cook model	31
3.3	Relationship between ultimate stress and maximum fracture strain . . .	40
3.4	Relationship between damage variable D and void volume fraction f .	40

3.5	Temperature dependency of fracture energy based on Eqs. (3.30) and (3.31)	45
4.1	Traction-separation relationships between the cohesive surfaces for six different temperatures	53
5.1	Specifications of DWTT used in the FE model	57
5.2	Illustration of meshing of the FE model	59
5.3	Finer mesh near the crack tip for accuracy of numerical analysis	59
5.4	Validation: Test results (Shim et al., 2010) and simulation results for X80 steel at room temperature (25°C)	61
5.5	Validation: Test results (Shim et al., 2010) and simulation results for X80 steel at a temperature of 0°C	61
6.1	Load displacement curves for six different temperatures	64
6.2	Illustration of steady state energy and maximum load on the DWTT specimen through a smoothed load-displacement curve obtained from a FE simulation at a temperature of -30°C.	65
6.3	Crack length vs. time ($T \geq 0^\circ C$)	67
6.4	Crack length vs. time ($T < 0^\circ C$)	67
6.5	Variation of crack speed with crack length	68
6.6	Measurement of CTOA	69
6.7	CTOA vs. crack length ($T \geq 0^\circ C$)	70
6.8	CTOA vs. crack length ($T < 0^\circ C$)	70
6.9	CTOD vs. crack length ($T \geq 0^\circ C$)	72
6.10	CTOD vs. crack length ($T < 0^\circ C$)	72
6.11	Empirical relation for temperature dependency of steady state CTOA	75
6.12	Empirical relation for temperature dependency of steady state CTOD	75

List of Abbreviations

Abbreviation	Full form
CZM	Cohesive Zone Model
CTOA	Crack Tip Opening Angle
CTOD	Crack Tip Opening Displacement
DWTT	Drop Weight Tear Test
EPFM	Elastic-Plastic Fracture Mechanics
FE	Finite Element
FEA	Finite Element Analysis
LEFM	Linear Elastic Fracture Mechanics
PS	Pipeline Steel
SMYS	Specified Minimum Yield Strength
SSC	Stress-Strain Curve
TM-CZM	Thermo-Mechanical Cohesive Zone Model

Chapter 1

Introduction

1.1 Pipeline's role in modern oil and gas industry

In the words of Mother Teresa, "To keep a lamp burning, we have to keep putting oil in it". Even though the sentence has deeper meaning, it also shows the quintessential need for oil and gas in the present world. Renewable sources of energy might show a promising new future. However, in the present world it is hard to imagine life without oil and gas, be it the need of a simple oil-lamp, essential commodities like medicine, clothing and plastic or huge aircrafts. Transportation, prepared food, industries, in fact everything that you can think of is directly or indirectly related to oil/gas in some way. This brings in the need for transportation of oil/gas to places where oil and gas are not abundant. Oil/gas transportation can be done in a number of ways. It can be broadly classified into land and marine transportation, which includes rail transport, road transport (oil trucks), pipelines, and ocean-going tankers and barges. However, for mass terrestrial transportation of oil, pipelines remain the most popular among other methods like road transport or rail transport. This is mainly because of the following reasons:

1. Pipelines are more cost-effective than the alternative transportation options.
2. They require significantly less energy to operate than operating trucks or rail and have a much lower carbon footprint.
3. It is not feasible to have a large-scale transportation of oil or natural gas by tanker truck or rail.
4. Pipeline transport (underground) of oil/gas is safer than road/rail transport due to more human involvement in the later case.
5. Road transport of oil/gas is always subjected to road and weather conditions, traffic etc. and the exact delivery time may vary, whereas in pipeline transport, the quantity of oil/gas transported is virtually independent of these factors.

According to Canadian Energy Pipeline Association (CEPA), there are enough underground natural gas and liquids pipelines in Canada to circle the Earth at the equator twenty times if laid end-to-end. The impact of the oil/gas industry on Canadian economy is huge, especially in Alberta. It is estimated that Canadians rely on natural gas and products made from crude oil to meet more than two-third of their energy needs. More than half the homes in Canada are heated by furnaces that burn natural gas. Natural gas specifically meets almost half of the energy needs to run the industries. Oil and gas are used to make hundreds of household and pharmaceutical products. In 2013 alone, the value of Canadian exports of crude oil and natural gas was more than 81 billion dollars. The pipeline and energy industries also provide employment to thousands of Canadians. With these points in mind, it is of utmost need that the safety and efficiency of pipeline transport of oil/gas is not compromised.

1.2 Historical importance of temperature dependence of fracture

Many catastrophic and fatal incidents in the past century caused due to temperature variation brought the attention to study temperature effect on materials in greater detail. The importance of temperature dependence of fracture process was felt way back in 1919 during the Great Boston Molasses Flood. Due to the sudden bursting of a molasses tank in Boston, there was a wave of molasses with a speed of upto 56 km/hr . There was 21 casualties and around 150 people injured during the incident. The smell of molasses was felt in the streets of Boston even decades later. The primary cause of the sudden bursting/fracture of the tank was attributed to a rapid fluctuation of temperature from below 0°C . This incident brought the attention to the fact that temperature effects can play a major role in failure of materials.

The second event which brought the whole concept of fracture mechanics into the picture was the incident of Liberty Ship failure. It is estimated that 2708 Liberty Ships were constructed between 1939 to 1945 and subsequently 1031 cases of damages and accidents were reported due to fracture (Kobayashi and Onoue, 1943). An interesting observation was that the warm waters of the South Pacific reported a significantly less number of fractures whereas most of the reported cases of ship failure were in the cold waters of the North Atlantic. These incidents and observations brought the importance of temperature dependence of fracture into the eyes of the scientific community.

1.3 Fracture of pipelines

Ruptures in pipelines has been a major cause of concern for linepipe transportation since ages. According to National Energy Board, Canada, from 1992 to 2012, thirty-

five cases of pipeline rupture has been reported to have occurred on Federally-regulated oil and gas pipelines in Canada. Rupture of pipelines can occur due to a variety of causes. The most predominant causes are listed in Table 1.1.

Table 1.1: Causes of pipeline rupture in Canada from 1992 to 2012 as reported by National Energy Board, Canada

Cause	Number of cases	Percentage
Cracking	12	34.3
Metal loss	10	28.6
Improper Operation	4	11.4
External Interference	3	8.6
Material, Manufacturing or Construction	3	8.6
Geotechnical Failure	2	5.7
Fire	1	2.8

According to reports published by National Energy Board, Canada from 1992 to 2012, 34.3% of the 35 reported cases of pipeline ruptures were caused due to cracking alone. There were reported cases of long propagating fractures in gas pipelines even in the 1950s. For example, a 5.6 km brittle fracture of a 24 inch pipeline was reported in Venezuela in 1958 and similarly a 13 km brittle fracture of a 30 inch pipeline in New Mexico in 1960. These incidents show that there still is a need for more advanced research on fracture initiation, as well as propagation for efficient and trustworthy design of pipelines.

1.4 Temperature effects on fracture of pipelines

From 1992 to 2012, about six cases of fracture of pipelines were recorded by National Energy Board, Canada. Interestingly, all six of these cases occurred in regions experiencing extremes of temperature. Further, the annual extreme minimum temperature for most of them goes below -40°C . This shows the importance of a more detailed analysis of the dynamic fracture in pipelines, with special consideration of temperature effects. This is the primary objective of the present research.

Temperature variation around pipelines even have a number of indirect effects. For example, with the increase in temperature, a higher rate of corrosion of the pipelines can occur. Typically between 60°C and 80°C , the corrosion rate reaches a maximum (Nešić, 2007). Temperature differences around pipelines can also induce or initiate significant environmental impacts (Széplaky et al., 2013).

1.5 Objectives of the thesis

The primary objective of the thesis is to present a temperature dependent cohesive zone model for pipeline steel (PS) and implement it through a finite element (FE) model that can explain and analyze the fracture behavior of PS in great detail. The pipeline material that has been used here is X80 steel. The detailed objective of the present research can be explained by the following points:

1. The first objective is to identify the key parameters of CZM and find its corresponding relationships with the known mechanical properties of the material under analysis. In order words, this objective aims to bridge the gap between classical solid mechanics and fracture mechanics by finding plausible inter-relations between them.

2. Once the key CZM parameters are identified, a temperature dependence of all the CZM parameters need to be established. To this end, the inter-relation of CZM parameters with the known mechanical properties is exploited. A temperature dependent and strain rate dependent constitutive strength model for PS has been established to achieve this objective.
3. Using the CZM parameters and their known temperature dependence, traction separation law (TSL) for PS at different temperatures are to be generated. The identification and generation of an appropriate TSL is not an easy task and forms a very crucial part of the present research.
4. The next objective is to generate a robust FE model based on the temperature dependent CZM for detailed fracture analysis of PS. The FE model was designed to simulate a Drop Weight Tear Test (DWTT).
5. Using the FE simulations, the temperature variations of the essential toughness parameters such as CTOA and CTOD are determined. The temperature dependency of crack length propagation and crack speed has also been identified to account for the steady state crack propagation.

Based on the temperature dependent CZM-based FE model, the present study thus enables us to obtain the dynamic fracture behavior of X80 steel at different temperatures.

Chapter 2

Background on pipeline steel

Materials used in line pipes are subjected to various combination of linear and transverse stress. A detailed knowledge of the mechanical behavior of materials is desired for an appropriate structural design of any kind. It helps engineers to determine the factor of safety for the design and to ensure that the deformation and deflection is not so huge so as to cause a failure of the structure. Most of the mechanical of materials indicate the response of the material to an applied load, either tensile, compressive or shear.

One of the objectives of the present research is to relate the cohesive zone model (CZM) parameters with the known mechanical properties of steel. To this end, a brief but robust idea of the mechanical behavior of pipeline steel (PS) is essential for our analysis. This chapter gives an introduction to these aspects of PS. This chapter also provides a brief idea about the different grades of PS, toughness testing methods and cohesive zone modeling of PS.

2.1 Pipeline steel

The need for transportation of oil/gas for long distance economically and effectively gave rise to the utilization of high strength steel for manufacturing pipelines. The primary benefit of using high strength steel for long distance pipelines is the reduced installation cost. This is because of the possibility of reduction of wall thickness to diameter ratio of the pipeline, which in turn, reduces the material cost (Cen, 2012).

In this section, the main grades of high strength PS that is in use in the pipeline industry will be introduced. The nomenclature of PS indicates the specified minimum yield strength (SMYS) of the steel in *ksi* which are displayed in Table 2.1. Table 2.1 also provides the chemical composition of these high strength steels (Cen, 2012, Coseru et al., 2013, G. Demofonti, G. Mannucci and Harris., 2004, Godefroid et al., 2014, Terada et al., 1997, Wang et al., 2001).

Table 2.1: Chemical composition of different grades of steel used for linepipes.

Grade	SMYS	Chemical Composition
	in <i>MPa</i> (in <i>ksi</i>)	
X52	359 (52)	0.07-0.2% C, 0.80% Mn, 0.27% Si, <0.01 % Mo etc.
X65	448 (65)	0.05-0.14% C, 1.0-1.5% Mn, 0.15-0.35% Si, 0.25 % Mo etc.
X70	482 (70)	0.06-0.10% C, 1.80% Mn, 0.39% Si, 0.302 % Mo etc.
X80	551 (80)	0.06-0.08% C, 1.7% Mn, 0.36% Si, 0.302 % Mo etc.
X100	689 (100)	0.05-0.06% C, 1.91-1.95% Mn, 0.31-0.35% Si, 0.30% Mo etc.

From the mechanical point of view, we are mainly interested in the increase in yield strength of PS which reduces the overall installation cost. However, this increase in yield strength reduces the ductility of the material. Failure of the material is expected to occur with lesser elongation as yield strength increases. Thus the choice of pipeline

material plays a very important role in the efficient and long-lasting functioning of the linepipes. In this work, we would be primarily restricted to the study of X80 steel.

2.1.1 X80 steel

X80 steel was first manufactured by Europipe in 1984 (Cen, 2012), which were used in several pipeline installation in Europe and North America. As seen from Table 2.1, the percentage of carbon in X80 steel is lower than the other lower grades, and thus contributed to the steel having excellent field weld-ability. This kind of steel is normally manufactured by thermo-mechanical rolling, followed by accelerated cooling.

2.2 Stress-strain curves for pipeline steel

A stress strain curve (SSC) for any material is the relationship between the extent of deformation and stress for that material. For quasistatic loading, simple stress-strain tests can be performed to determine the stress-strain relationship for a material. One of the most common and universally accepted stress strain test is the uniaxial tensile test (William D. Callister, 2001). In such a test, a specimen of the material is subjected to a gradually increasing load that is applied uniaxially along the axis of the specimen. The testing machine ideally elongates the specimen at a constant rate until the point of complete fracture, and simultaneously records the instantaneous applied load and resulting elongation. The engineering SSC can be easily obtained from the recorded data for the specimen. A typical circular tensile test specimen is shown in Figure 2.1. A number of SSCs for commercially available PS such as X70, X80 and X100 are shown in Figure 2.2. These curves have been assembled from different research works (Bai et al., 2014, Han et al., 2009, Qiu, 2010, Rudland et al., 2003, Wang et al., 2001, Wilkowski et al., 2008).

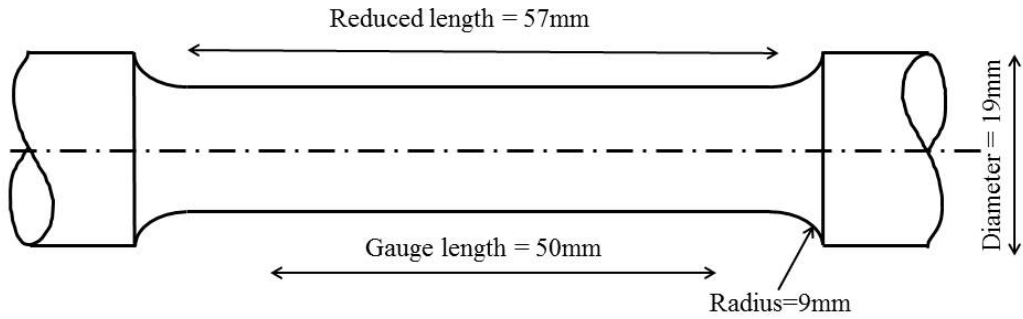


Figure 2.1: Standard specimen for uniaxial tensile test with circular cross-section (William D. Callister, 2001).

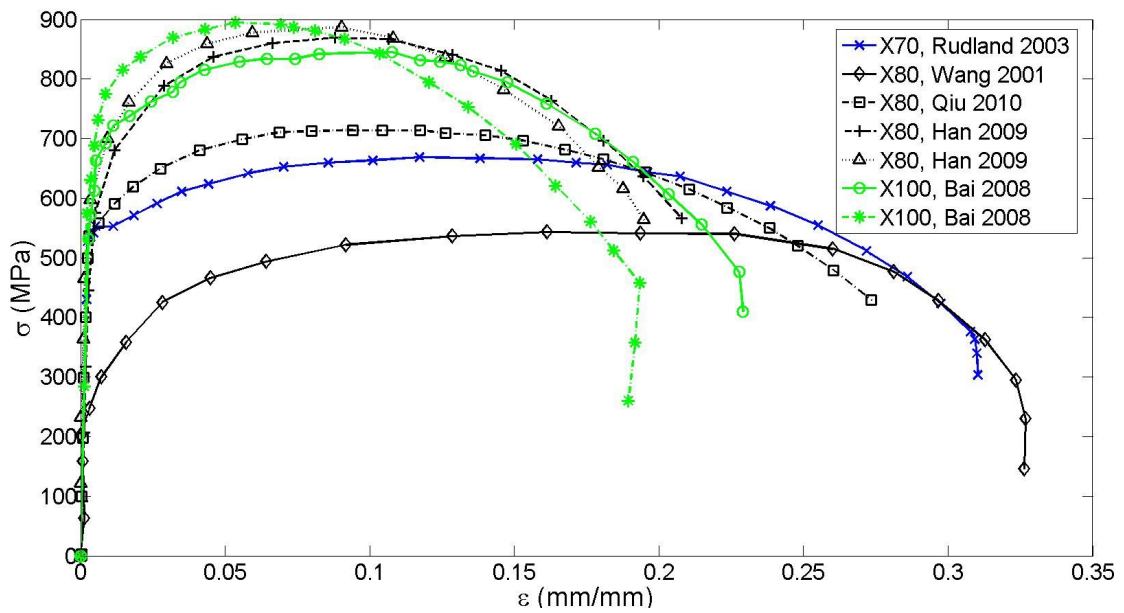


Figure 2.2: Stress strain curve for PS for room temperature.

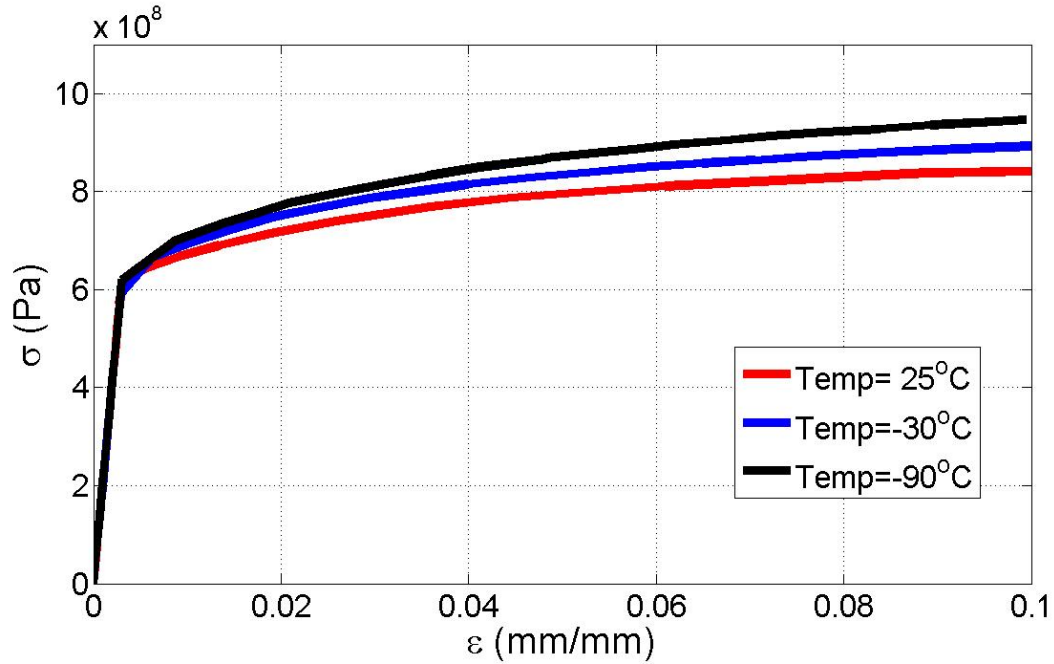


Figure 2.3: True stress strain curves at three different temperatures for X80 steel (Akselsen et al., 2012, Jung et al., 2013, Ren and Ru, 2013).

2.2.1 Temperature-dependent stress-strain curves for pipeline steel

The stress strain behavior for the same material vary significantly with temperature. Obtaining SSCs at different temperatures experimentally is a very challenging task. This is because a constant temperature has to be maintained throughout the experiment. Very low or very high temperatures would impair the involvement of human workers near test setup. Also this is expected to produce errors in reading, mainly due to the thermal damage and thermal expansion or contraction of the instruments involved. In spite of the challenges, SSCs at different temperatures for X80 have been presented by Xu et al. (2010), Jung et al. (2013) and Akselsen et al. (2012). Figure 2.3 shows three true SSCs at different temperatures that is relevant to the present research.

2.2.2 Relationship between ultimate stress and temperature

A huge number of research (Anderberg, 1988, Burns and Z. J. Bilek, 1973, Chen et al., 2006, Johnson and Cook, 1983) has been done to relate tensile strength and yield strength with temperature for steel. Almost unanimously in all these analysis, we see a decrease in strength of materials with increase in temperature. Kotilainen (1979) presented a mathematical model, known as Yaroshewich-Ryvkina model (Eq.(2.1)) to capture the temperature dependency of ultimate tensile strength.

$$\sigma_u = a + b \exp(-cT) \quad (2.1)$$

where σ_u and T are ultimate tensile strength and temperature in absolute scale respectively. a , b and c are constants that could be determined by matching the curve with known data points. The values of the constants for X80 steel were found to be $a = 750 \text{ N/mm}^2$, $b = 1227 \text{ N/mm}^2$ and $c = 0.0126 \text{ K}^{-1}$ respectively. An order of magnitude comparison of the constants were also performed with results from Shin et al. (2006) to further confirm the validity of this equation for PS. Figure 2.4 provides deeper insight into the above method. In the figure the red circles represent the data points obtained from the literature for X80 steel (Akselsen et al., 2012, Ma et al., 2014, Ren and Ru, 2013, Xu et al., 2010) whereas the blue dotted line represents the predictions of σ_u by Yaroshewich-Ryvkina model.

2.3 Fracture toughness

Fracture toughness is a generic term which represents resistance of a material to crack extension. In order words, fracture toughness is a material property that is used to quantify the resistance of a material to fracture and crack growth. Fracture toughness

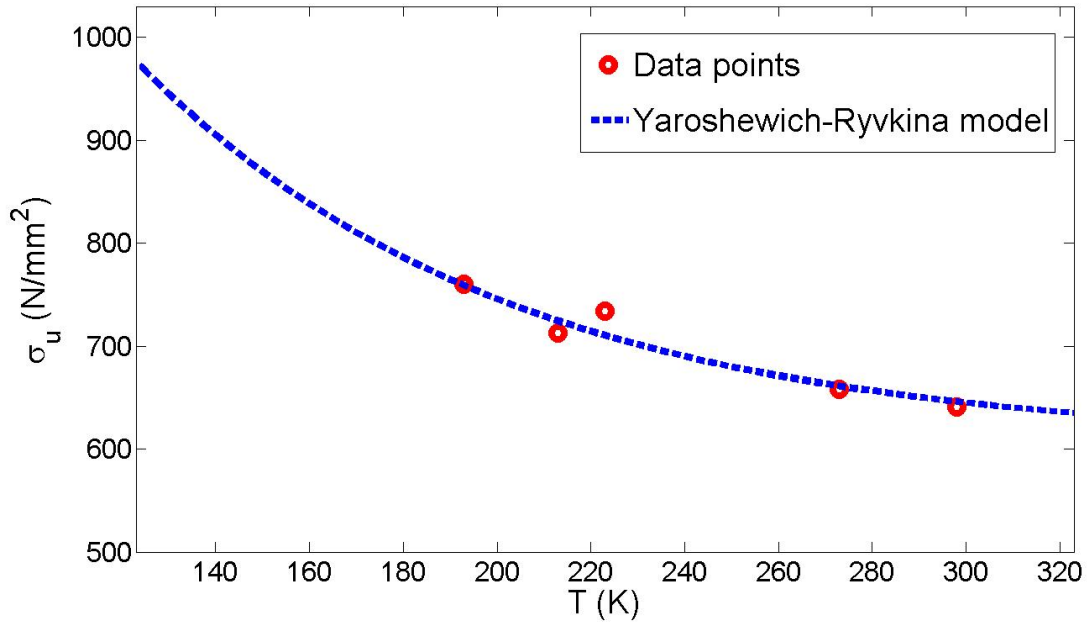


Figure 2.4: Curve fit of Yaroshewich-Ryvkina model relating ultimate strength and temperature for PS

is quantified by various toughness parameters such as stress intensity factor, fracture energy, J-integral, energy release rate, CTOD, CTOA and so on. Many of these parameters can be inter-related for classical linear elastic fracture mechanics (LEFM) or elastic-plastic fracture mechanics (EPFM). However, for CZM approach, this inter-relation becomes more difficult. In the present problem, we will represent fracture toughness by fracture energy per unit area or simply fracture energy.

2.3.1 Toughness parameters

Many toughness parameters are used to quantify the resistance of a material to growth of a crack. Classically from the point of view of LEFM, stress intensity factor was the most primitive toughness parameter. To overcome the problem of singularity at the crack tip, EPFM was introduced which used J-integral or energy release rate as the toughness parameter. Another toughness parameter frequently used in fracture

mechanics is fracture energy (or fracture energy per unit area). Fracture energy has the units of J/m^2 . Other important toughness parameters are crack tip opening angle (CTOA) and crack tip opening displacement (CTOD). In this thesis we will mainly deal with fracture energy, CTOA and CTOD as the toughness parameters.

2.3.2 Temperature dependence of fracture toughness

Based on temperature dependency of fracture toughness of most materials, they can be divided into three different temperature zones.

1. Brittle region (Region I): Fracture toughness increases slightly with increase in temperature in this region. If these small variations are neglected, then the fracture toughness in brittle region can be considered as constant, which is generally referred to as the lower shelf fracture toughness.
2. Brittle-to-Ductile transition region (Region II): There is a very rapid change in fracture toughness in this region with considerable scatter in the measured values of fracture toughness during tests.
3. Ductile region (Region III): In this zone too, there is a very gradual increase in fracture toughness with increase in temperature. Similar to the brittle region, we can refer to upper shelf fracture toughness for this region, considering fracture toughness to be constant.

Figure 2.5 illustrates the three regions of varying temperature dependency of fracture toughness (Kaminskii and Galatenko, 1999).

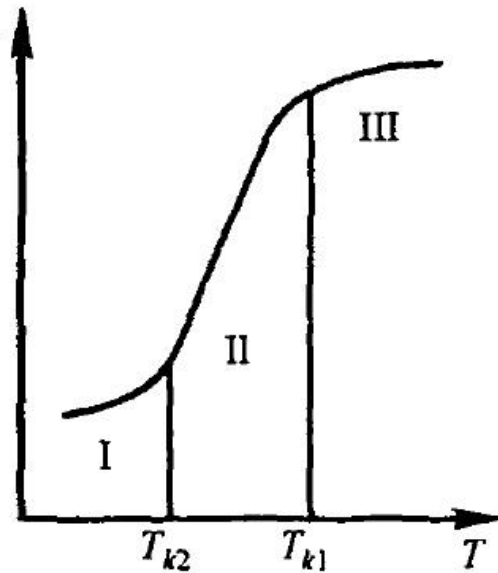


Figure 2.5: Variation of fracture toughness with temperature (Kaminskii and Galatenko, 1999)

2.4 Fracture toughness testing

There are a number of tests that are performed to find the various toughness parameters for steel. Here we will discuss two of the most widely used tests for toughness characterization, namely Charpy impact test and Drop Weight Tear Test (DWTT). The success of these two test in industrial applications owes to their lower operating cost and ease of operation when compared to other toughness tests.

2.4.1 Charpy impact test

The invention of Charpy impact test dates way back to 1901 when G. Charpy, a French scientist proposed a pendulum test that measured the energy of separation in metallic specimens. Charpy impact test measures the amount of impact energy required for complete fracture of a material. Impact energy serves as a measure of the toughness of the material. The Charpy test is usually performed on a simple pre-notched specimen

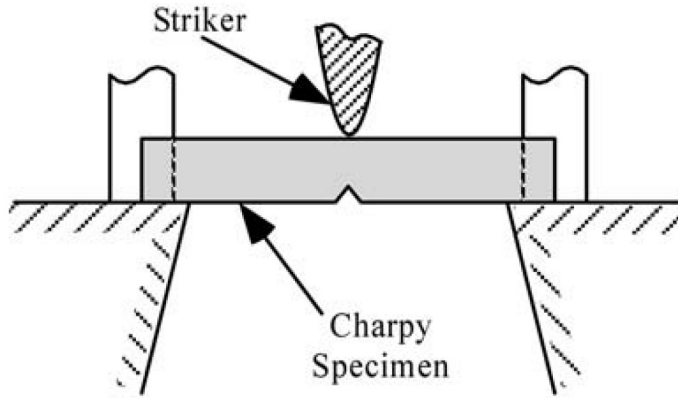


Figure 2.6: Schematic of Charpy impact test (Anderson, 2005)

of dimensions $10\text{ mm} \times 10\text{ mm} \times 55\text{ mm}$. The Charpy specimen is impacted by a heavy pendulum and the impact energy is recorded corresponding to complete fracture of the specimen. Charpy test is specified in ASTM Standard E 23. This test is also used to analyze brittle to ductile transition of a material. Owing to its compact size and quickness of operation, this method is widely popular in industry.

2.4.2 DWTT

DWTT was developed in the early 1960s to overcome the limitations of the other toughness tests such as Charpy test and Pellini drop weight test. DWTT is specified in ASTM Standard E 436. It is simply a three-point bending test where the hammer strikes the specimen at a particular velocity until fracture. Figure 2.7 provides a deeper insight of the test and also shows the dimensions of a typical DWTT specimen according to ASTM Standard 436.

The primary advantages of DWTT over conventional Charpy impact test can be innumeraated as follows:

1. DWTT has better agreement with actual fracture scenarios in pipelines. This can be attributed to the fact that the DWTT specimen, in general, has the same

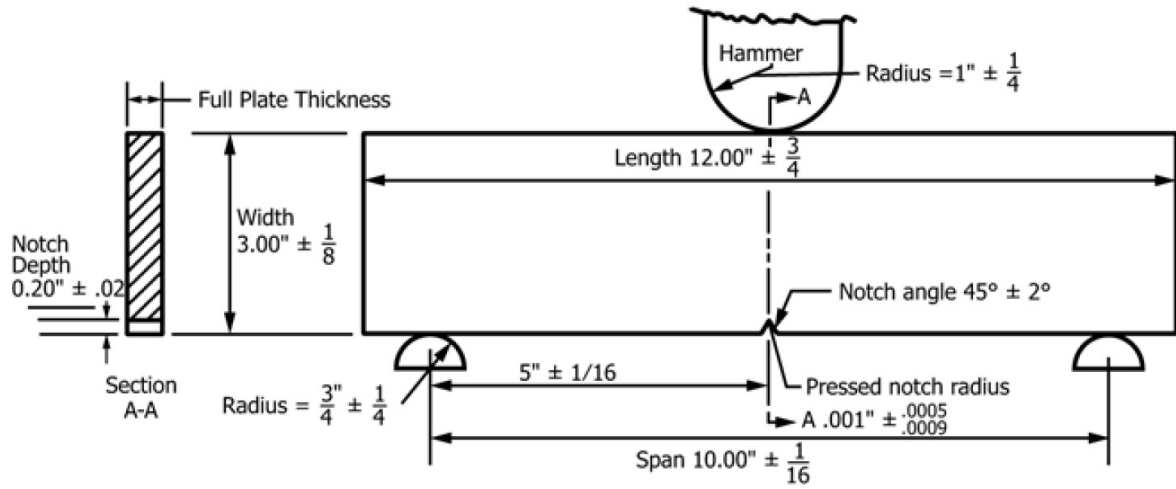


Figure 2.7: Schematic of DWTT (ASTM Standard E 436)

thickness at that of a linepipe. Charpy test, in contrast, is not of the full thickness of a linepipe.

2. Charpy Test can have a maximum fracture speed much smaller than that seen in actual pipeline fractures, whereas DWTT can go quite close to the actual fracture speed encountered (Shim et al., 2010).
3. In the Charpy test, the smaller length of the fracture path does not usually allow the steady-state fracture growth. In DWTT, steady-state fracture propagation is observed for a significant length of the ligament and hence detailed analysis of steady state crack growth and steady-state toughness parameters is possible.
4. A normal Charpy test specimen has a blunt notch whereas DWTT specimens use a sharp V-notch at an angle of 45°. A sharp crack is more commonly seen in pipeline fractures.

Due to the above reason, the present finite element (FE) model was made based on DWTT, rather than Charpy impact test.

2.5 Cohesive zone model (CZM)

Cohesive zone was an initiative in fracture mechanics introduced in order to overcome the problem of stress singularity faced at the crack tip while applying classical fracture mechanics theory like LEFM. The assumption of a perfectly sharp crack and linear elastic material property accounted for causing the stress at the crack tip to become infinitely large. EPFM overcomes this problem of singularity by assuming plastic material behavior. In cohesive zone modeling, the problem is overcome by the assumption of a cohesive zone near the crack tip along the direction of crack propagation. A cohesive zone is formed by two cohesive surfaces which are held together by cohesive traction, or simply traction. A cohesive law governs the interaction between the two bound cohesive surfaces, which is also popularly known as traction-separation law (TSL). Identifying an appropriate traction-separation relationship for the material under study is one of the most fundamental and most challenging task of cohesive zone modeling. Figure 2.8 illustrates a CZM for one-directional crack growth. In the figure, the length of the cohesive zone from the crack tip is represented by a d . At a distance of d from the crack tip, complete fracture of the material occurs.

In order to implement CZM in finite element, the two cohesive surfaces of the CZM needs to be pre-defined. In other words, the direction and length of crack propagation has to be pre-defined for a FE model to be produced.

2.5.1 Existing CZM

After the initial introduction of non-linear material failure by Elliott (1947), Barenblatt (1959, 1962) presented the concept of CZM to analyze the fracture of brittle materials. Dugdale (1960) further used a similar CZM to study the size of the plastic zone in cohesive zone modeling and yielding at the crack tip. Dugdale introduced the concept

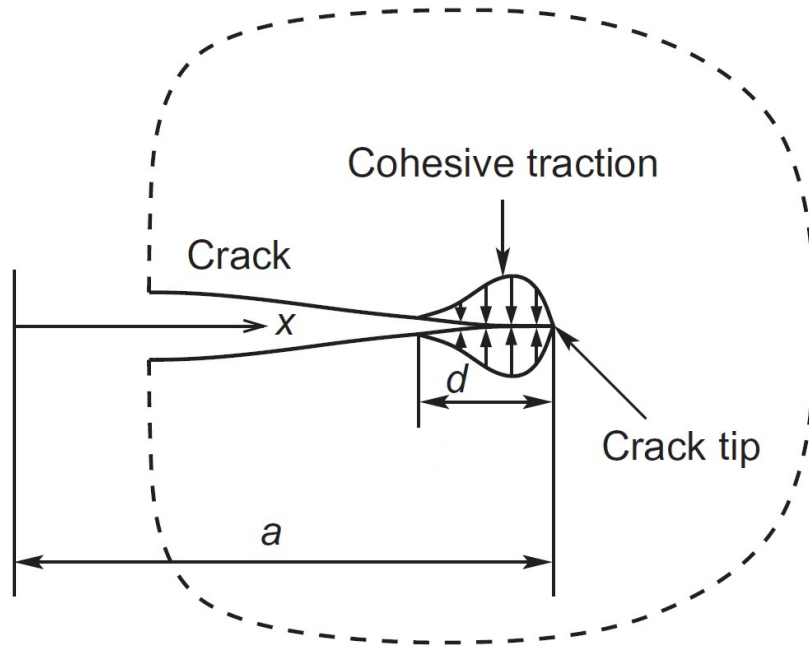


Figure 2.8: Cohesive zone modeling near crack tip (Sun and Jin, 2012): a is crack length, x is the crack propagation direction, d is cohesive zone length.

of application of CZM to study ductile fracture in steel.

Since then, many different TSLs have been suggested by researchers which are found to be effective for different materials. In fact, traction separation law was developed from the simple one-dimensional case to a three-dimensional form to account for complicated material behavior. However, in the present problem we will stick to one dimensional TSL to produce a FE model of DWTT since the crack essentially propagates in one direction for DWTT. Some of the frequently used traction-separation relations are listed below (Elices et al., 2002, Park and Paulino, 2013, Volokh, 2004):

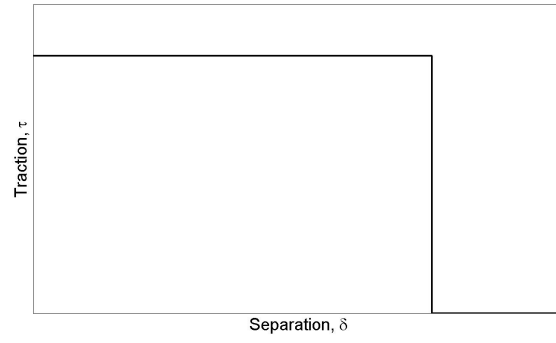
1. constant
2. linearly decreasing
3. bilinearly decreasing
4. linearly increasing and linearly decreasing

5. non-linear
6. linearly increasing and non-linearly decreasing
7. cubic polynomial
8. trapezoidal
9. smoothed trapezoidal

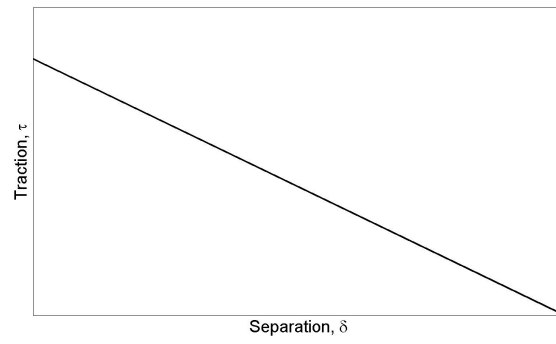
Figure 2.9 further illustrates these different kinds of TSL that are frequently used by different researchers. In the present model a linearly increasing, non-linearly decreasing type of TSL (Figure 2.9f) has been implemented in accordance with Ren and Ru (2013) and Yu and Ru (2015) model, which achieved agreeable results for PS.

2.5.2 Existing temperature dependent CZM

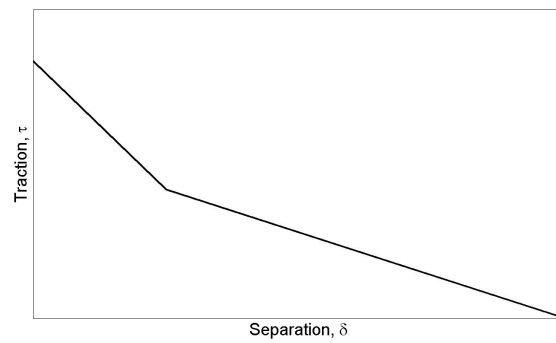
Many temperature dependent CZMs exist in the literature for polymers and other complex material which are very sensitive to temperature changes. Coupled thermo-mechanical CZM (TM-CZM) have been frequently used over the past decade to study the temperature dependent mechanical behavior (Costanzo and Allen, 1993, Fagerström and Larsson, 2008, Shimizu et al., 2007). TM-CZM was even used to study fatigue of solders in electronic chip packages subjected to active power cycling (Benabou et al., 2013). However such a temperature dependent CZM is relatively rare for steel. For PS, no such CZM has been found to the best of my knowledge. The thesis aims to report such a temperature dependent CZM for PS to fill this gap in the present literature.



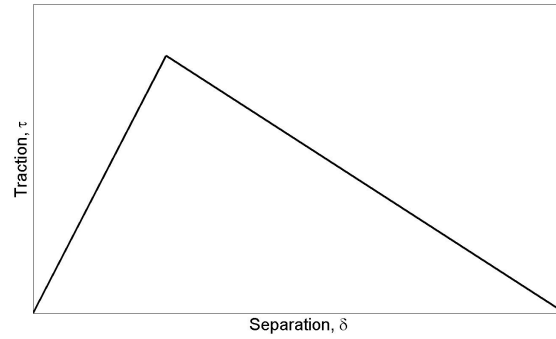
(a) Constant



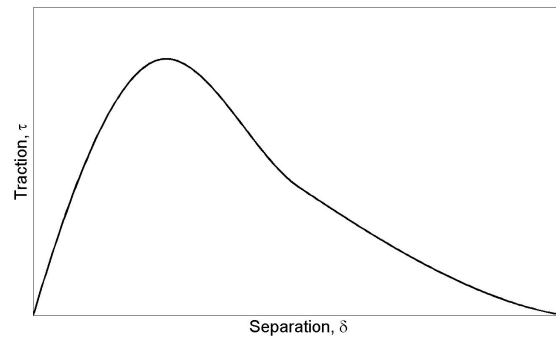
(b) Linearly decreasing



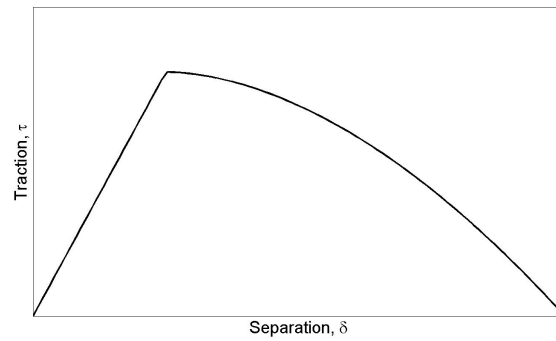
(c) Bilinearly decreasing



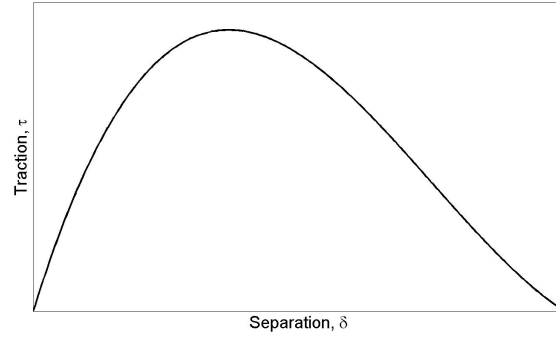
(d) Linearly increasing and linearly decreasing



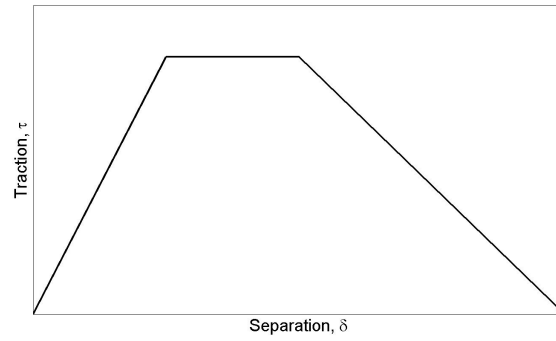
(e) non-linear/exponential



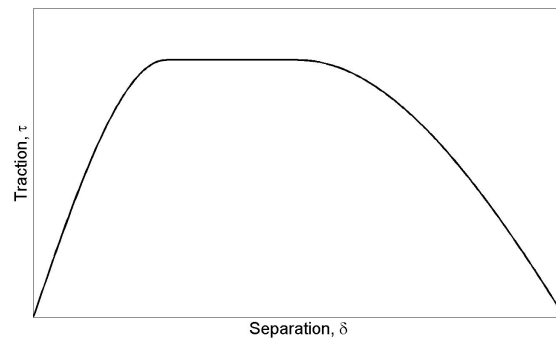
(f) linearly increasing and non-linearly decreasing



(g) Cubic polynomial



(h) Trapezoidal



(i) Smoothened trapezoidal

Figure 2.9: Different forms of the traction-separation relationships used for cohesive zone modeling

Chapter 3

Temperature dependency of mechanical properties of pipeline steel

A deeper understanding of the mechanical properties of pipeline steel (PS) is imperative to analyze the temperature effects on dynamic fracture of PS. Mechanical properties of any material includes stress strain behavior, fracture behavior, hardness, ductility and so on. A introduction to the important mechanical behavior of PS has been provided in the previous chapter. In the present chapter, we will focus on the temperature dependency of stress strain behavior and fracture energy for PS. This is vital for the proper calibration and interpretation of the essential cohesive zone model (CZM) parameters.

3.1 Modified Johnson-Cook strength model

For generating a temperature-dependent CZM, it is important to obtain a constitutive model for true stress and strain. Johnson and Cook ([Johnson and Cook, 1983, 1985](#)) proposed such a temperature dependent and strain rate dependent model which was widely accepted by the scientific world.

3.1.1 Original Johnson-Cook model

The original Johnson-Cook strength model (Johnson and Cook, 1985) was formulated to relate true stress with plastic strain, for applications in numerical computations. The wide popularity of this model can be attributed to the simplicity of the model. It was later used in a wide number of applications. Many researchers further implemented minor modifications to the model to improve on its ability to reproduce true stress strain curves (SSCs). The Johnson-Cook constitutive model in its original form can be stated as:

$$\sigma = \underbrace{(A + B\epsilon_p^n)}_{\text{quasi-static term}} \overbrace{(1 + C \ln \dot{\epsilon}^*)}^{\text{strain rate term}} \underbrace{(1 - T^{*m})}_{\text{temperature term}}, \quad (3.1)$$

where σ is the true stress, ϵ_p is the plastic strain, $\dot{\epsilon}^*$ is the dimensionless equivalent plastic strain rate and T^* is the non-dimensional temperature. Mathematically $\dot{\epsilon}^*$ can be expressed as:

$$\dot{\epsilon}^* = \frac{\dot{\epsilon}}{\dot{\epsilon}_0}, \quad (3.2)$$

where $\dot{\epsilon}$ is the actual plastic strain rate and $\dot{\epsilon}_0$ is the reference strain rate. Similarly, T^* can be expressed as:

$$T^* = \frac{T - T_{room}}{T_{melt} - T_{room}}, \quad (3.3)$$

where T is the actual operating temperature in absolute scale, T_{room} is the room temperature and T_{melt} is the melting point temperature of PS.

There are five material constants in Eq. (3.1). A , B and n are constants related to the static or quasistatic stress-strain data. C and m determines the strain-rate

sensitivity and temperature sensitivity of the material respectively.

The equation essentially consists of three multiplicative terms. The quasistatic term corresponds to the static or quasistatic behavior of the material, and can be related to uniaxial tensile test data at room temperature. The other two multiplicative terms describes the strain rate dependency and temperature dependency of the material under consideration.

Assumptions

The main assumptions for the Johnson-Cook model for modeling mechanical behavior of matter are listed below:

1. Isotropic hardening is considered.
2. This constitutive model operates in the classical elastoplastic framework. Elastic constitutive model defines the elastic response, a yield criterion defines the delimitation of the elastic regime. The plastic response is determined by Eq. (3.1).
3. This model updates the true stress only and not the volumetric response of the material.

3.1.2 Modification for low temperature applications

In the present sub-section, we are only concerned about the temperature term of the Johnson-Cook model, and the strain rate dependency of the model is not being considered for simplicity of explanation. Thus the numerical value of C is set to zero for this sub-section, and Eq. (3.1) now becomes:

$$\sigma = (A + B\epsilon_p^n)(1 - T^{*m}), \quad (3.4)$$

One of the major shortcomings of the model is the fact th Eq. (3.4) is functional only for temperatures higher than the room temperature. This incapability of the model to generate low temperature true SSCs triggered a number of modifications to the model by different researchers to account for low temperature applications. Here we will discuss about a few of the most significant modifications of the temperature term found in the literature.

Meyers et al. (1995) modified the Johnson-Cook model using a exponential function of temperature as shown in Eq. (3.5). This modified model was primarily used for tantalum.

$$\sigma = (A + B\epsilon_p^n)e^{-m(T-T_{melt})}. \quad (3.5)$$

Here m is a material constant that parameterizes the thermal softening for the material and all the other terms have the same meaning as Eq. (3.4).

Even though the above modified model seemed to be effective for tantalum, it did not work out well for PS and other materials such as brass (Wang et al., 2004). This is mainly because of the fact that the temperature term in Eq. (3.5) produces a non-zero value at room temperature, and jeopardizes the validity and reasonability of the other constants used in the model. This model is hence more applicable when the operating temperature is very high and close to the melting point temperature T_{melt} . This model was also discarded by Wang et al. (2004) since it did not account for the non-identical strain hardening behavior due to strain-rate effects.

In order to use the Johnson-Cook model for a wide range of temperatures, (Hou and Wang, 2010) introduced a different modification as shown in Eq. (3.6). The modification was designed to study the plastic response of Mg-10Gd-2Y-0.5Zr alloy

over a wide range of temperature, both higher and lower than room temperature.

$$\sigma = (A + B\epsilon_p^n) \left(1 - m \frac{e^{T/T_{melt}} - e^{T_{room}/T_{melt}}}{e - e^{T_{room}/T_{melt}}} \right). \quad (3.6)$$

This method compromised on the idea of the present research to maintain a simplistic approach to the problem. Another recent work (Qingdong et al., 2014) tried a yet different approach where, unlike the assumption in Johnson-Cook model, the variations of hardening part and parameter A (which is equal to yield stress σ_0 , explained in details in section 3.1.5) are considered asynchronous with variations in temperature. Mathematically, they proposed the following modified model:

$$\sigma = A(1 - pT^{*m}) + B\epsilon_p^n. \quad (3.7)$$

where the parameters B and n are both functions of T^* , and p and m are the parameters controlling temperature dependency of parameter A . While this approach might seem a good simple approach at first look, the dependency of B and n on temperature makes this model unable to be implemented for the present problem. Moreover, there is less justification in making a strength model where the material parameters itself are temperature dependent and needs to be determined separately for each temperature from test results or by curve fitting.

Thus, these methods too were found to be ineffective for PS. As a result, a simplified modification of the model was proposed as shown:

$$\sigma = (A + B\epsilon_p^n)(1 - \lambda|T^*|^m) \quad (3.8)$$

where λ is described by:

$$\lambda = \begin{cases} 1 & : T = T_{room} \\ T^*/|T^*| & : T \neq T_{room} \end{cases} \quad (3.9)$$

λ essentially functions as a parameter controlling the sign before non-dimensional temperature T^* . When the operating temperature T is more than T_{room} , λ is equal to +1 and when the operating temperature T is less than T_{room} , λ is equal to -1.

Verification by matching with true strain-strain curves

Eq. (3.8) gives the final modification for temperature term for Johnson-Cook model. The model has been matched up with test results that were previously shown in Figure 2.3. Figure 3.1 illustrates the comparison. The model shows a small deviation near the beginning of the plastic zone. However, since the model will be ultimately used to find the value of maximum true fracture stress, this discrepancy does not cause any significant impact on the overall accuracy of the CZM.

3.1.3 Modification for strain rate term

Having finalized the temperature term of the Johnson-Cook strength model, now we turn our focus on the strain rate term. There are several drawbacks in the original formulation. Firstly, the model is not well defined for very small strain rate. In other words, the logarithmic function $\ln(\dot{\epsilon}_p^*)$ approaches a value of negative infinity when the strain rate is very small. Secondly, it causes unwanted effects when $\dot{\epsilon}^* < 1$. Thirdly, many ductile metals has a higher sensitivity towards strain rate than that estimated by Eq. (3.1) (Rule and Jones, 1998). To develop on the above mentioned drawbacks, a wide number of modifications for the strain rate term was suggested by

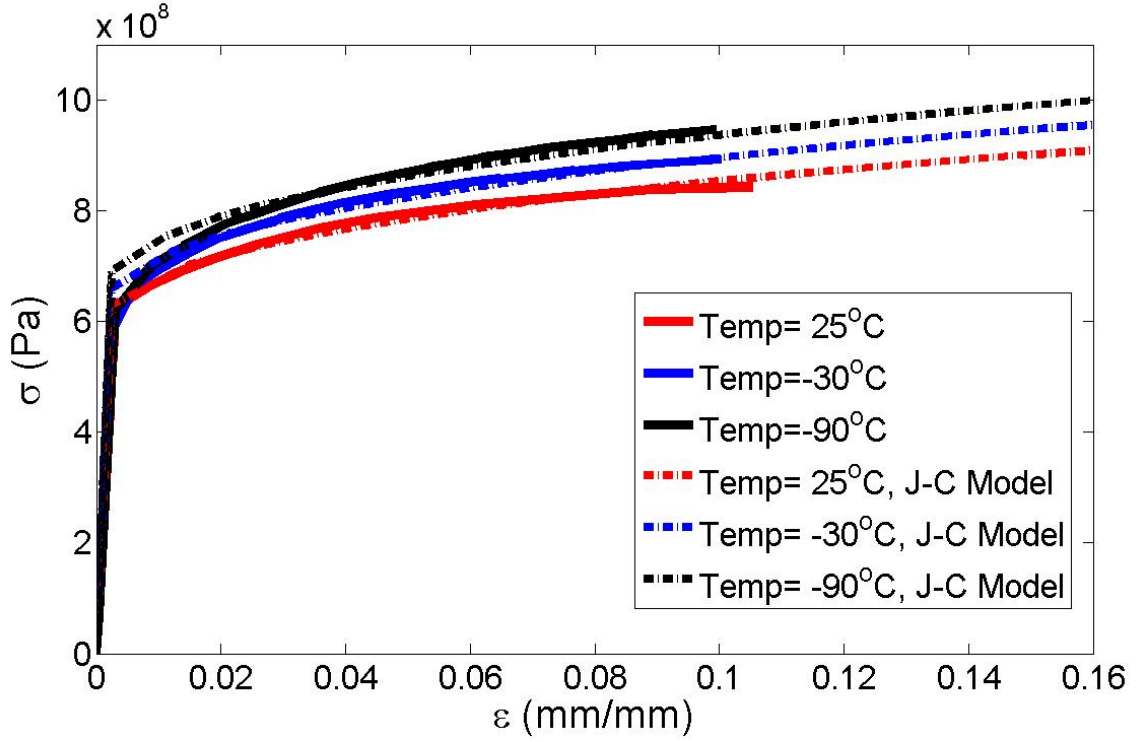


Figure 3.1: Verification of modification of temperature term in Johnson-Cook model

different researchers. [Holmquist and Johnson \(1991\)](#) introduced a modified strain rate dependency term as shown (Here the temperature term has not been shown for ease of explanation):

$$\sigma = (A + B\epsilon_p^n)(\dot{\epsilon}^*)^C, \quad (3.10)$$

Even though this model seems very simple and usable, the problem of discrepancy for very small strain rate does not completely go away. [Wang et al. \(2004\)](#) suggested a more complicated model where the change in temperature only affects the strain hardening part whereas it has no effect on yield strength, represented by parameter A (details in sub-section [3.1.5](#)).

$$\sigma = A(1 + C_1 \ln \dot{\epsilon}_p^*) + B\epsilon_p^n(1 + C_2 \ln \dot{\epsilon}^*)e^{-m(T-T_m)}, \quad (3.11)$$

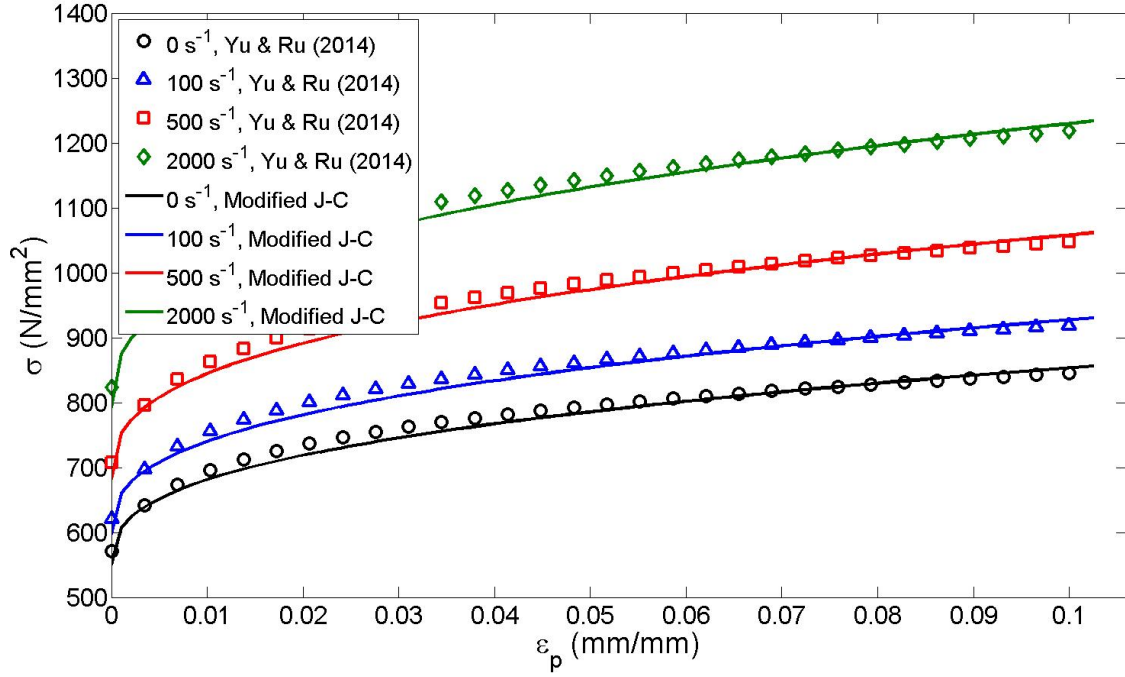


Figure 3.2: Verification of modification of strain rate term in Johnson-Cook model

Børvik et al. (2001) and Clausen et al. (2004) used a still different, but simple form of modification as shown in the following equation:

$$\sigma = (A + B\epsilon_p^n)(1 + \dot{\epsilon}^*)^C \quad (3.12)$$

After a careful trial of the above mentioned models, it was found that Eq. (3.12) to be most suitable for PS.

Verification by matching with true strain-strain curves

The final modification for strain rate term for Johnson-Cook model is given by Eq. (3.12). The model has been matched up with results from Yu and Ru (2015) illustrated by Figure 3.2. This modified model shows very good match with the available stress-strain data for X80 steel.

3.1.4 Final modified form of Johnson-Cook model

In regard to the previous arguments, the final form of the modified Johnson-Cook model to be used in the current research work can be expressed as:

$$\sigma = (A + B\epsilon_p^n)(1 + \dot{\epsilon}^*)^C(1 - \lambda|T^*|^m) \quad (3.13)$$

where all the parameters have been previously defined. To plot the actual SSC along with the elastic part, the maximum elastic true stress $\sigma_{e,max}$ has to be identified. $\sigma_{e,max}$ is numerically equal to the true stress when plastic strain is zero.

$$\sigma_{e,max} = \sigma|_{\epsilon_p=0} \quad (3.14)$$

Henceforth, the maximum elastic strain can be defined as:

$$\epsilon_{e,max} = \sigma_{e,max}/E. \quad (3.15)$$

For the elastic part ($\epsilon_e \leq \epsilon_{e,max}$),

$$\begin{aligned} \epsilon &= \ln(1 + \epsilon_e) \\ \sigma &= E\epsilon(1 + \epsilon_e) \end{aligned} \quad (3.16)$$

For the plastic part ($\epsilon_e > \epsilon_{e,max}$),

$$\epsilon = \epsilon_{e,max} + \epsilon_p \quad (3.17)$$

The true plastic stress can be obtained from Eq. (3.13)

In this study, it has been assumed that for PS, the change in Young's modulus E

is negligible with change in temperature and change in strain rate. Hence E has been assumed to be constant throughout.

3.1.5 Calibration of the modified strength model

The Johnson-Cook strength model is an excellent mathematical model that provides us the value of true stress at any known value of plastic strain, strain rate and temperature. However it is very important that the equation be properly calibrated for reliable results. As evident from the equation, the numerical value of true stress is the product of three independent factors representing strain hardening, strain rate and temperature. This has made the calibration of the model easier due to the fact that the three different factors can be matched up separately to uniaxial test data to find the values of the constants.

The calibration of the original Johnson-Cook model can be done in a number of ways. [Holmquist and Johnson \(1991\)](#) and [Gambirasio and Rizzi \(2014\)](#) elaborately explained most of the significant calibration strategies. In the present research, a modified form of the original LYS (Lower Yield Stress) calibration strategy has been implemented to obtain numerical values of the material constants. The modification in the calibration technique needed to be used because of the modifications (Eq. (3.13)) introduced to the original Johnson-Cook strength model (Eq. (3.1)). The necessary test data required to initiate the calibration of the model are:

1. Stress strain curve at room temperature, T_{room} and at static or quasistatic state ($\dot{\epsilon} \simeq 0$),
2. Stress strain data at a temperature different from room temperature T_{room} and at quasistatic state, and
3. Stress strain relationship at a non-zero strain rate, but at room temperature.

There are in all eight unknown parameters in the modified Johnson-Cook model, including the material constants. Calibration of the modified Johnson-Cook model means accurately determining the values of the five material constants (A , B , C , n and m). There are four steps involved to properly calibrate the model.

1. *Constant quantities and reference parameters*

The very first step towards calibrating the modified Johnson-Cook model is identifying the constant quantities and reference parameters. The reference temperature for modified Johnson-Cook model is taken as room temperature T_{room} (Johnson and Cook, 1985). For the present analysis, T_{room} was take equal to 25°C in centigrade temperature scale (298 K in absolute scale). The melting point temperature T_{melt} for X80 steel was approximated from iron-carbon phase diagram. T_{melt} was taken equal to 1500°C in centigrade temperature scale (1773 K in absolute scale).

The reference strain rate $\dot{\epsilon}_0$ needs to be carefully chosen so that the model has the accurate strain rate sensitivity. The value of $\dot{\epsilon}_0$ was taken equal to 100 s^{-1} , which was found to be in accordance with the reference strain rate value assumed by Yu and Ru (2015).

2. *Calibration of quasistatic parameters*

The first term in Eq. (3.13) may be referred to as the quasistatic term. The three quasistatic parameters, namely, A , B and n can be found out by fitting with a true SSC obtained from uniaxial tensile test at room temperature. This confirms that the non-dimensional temperature T^* is equal to zero and thus the temperature term is equal to one. Since the uniaxial tensile test is performed at a quasistatic state, hence it is reasonable to assume $\dot{\epsilon} \simeq 0$. This further ensures that the strain rate terms become equal to one, and the Johnson-Cook model

takes the following form:

$$\sigma = (A + B\epsilon_p^n) \quad (3.18)$$

The material constant A is actually equal to the yield stress of the material at room temperature T_{room} , represented by σ_0 (Johnson and Cook, 1983). The other two parameters, B and n determine the successive hardening of the material. These parameters can be found out by fitting the experimental data. In the present analysis, this has been done with the help of MATLAB R2014a.

3. Calibration of temperature term

The material constant controlling the strain rate dependency is the exponent m . This step involves comparison with test results conducted at quasi-static state and at a temperature different from room temperature. Quasi-static state ensures that $\dot{\epsilon} \simeq 0$ and thus the strain rate term can be taken equal to zero. With this deduction, we can obtain the value of the material constant m from the following equation:

$$m = \frac{\ln\{\sigma/(A + B\epsilon_p^n)\}}{\ln(1 - \lambda|T^*|^m)} \quad (3.19)$$

The value of m is found to be equal to 0.81, which is well within the range of values of m suggested by Johnson and Cook (1983, 1985). This value also matched quite well with Børvik et al. (2001), Clausen et al. (2004).

4. Calibration of strain rate term

The material constant controlling the strain rate dependency is C . The easiest way to calibrate the strain rate term is to compare with experimental SSCs at

reference temperature and non-zero strain rate using the following equation:

$$C = \frac{\ln\{\sigma/(A + B\epsilon_p^n)\}}{\ln(1 + \dot{\epsilon}^*)} \quad (3.20)$$

C was found to be equal to 0.12, and matches with the material constant used by [Yu and Ru \(2015\)](#) used in a similar model.

The details of the other procedures has been reported by [Gambirasio and Rizzi \(2014\)](#) and beyond the scope of the present thesis.

3.2 Maximum true stress

The importance of identifying maximum true stress goes towards obtaining a definite temperature dependent traction-separation law (TSL) for the CZM for fracture analysis of PS. This will be elaborately explained in Chapter 4. The maximum true stress for any material is essentially equal to the true stress experienced by the material at the point of complete fracture. This maximum value of true stress at any temperature can be represented by σ_f and can be obtained from the modified Johnson-Cook model using Eq. (3.13). It is to be noted that by σ_f , the true fracture stress in quasistatic state is meant. Thus strain rate $\dot{\epsilon} \simeq 0$ and the strain rate term equals one.

To find the maximum true stress σ_f at any temperature, the maximum fracture strain at the same particular temperature should be known. However, not many true SSCs for the present grade of PS could be obtained even after a detailed literature survey. To this end, an empirical relationship between ultimate stress and maximum fracture strain has been obtained as explained below.

3.2.1 Relationship between ultimate stress and maximum fracture strain

A thorough literature survey reveals that as the ultimate strength or yield stress increases, there is a corresponding decrease in maximum fracture strain for most metals. The main reason for such an observation is due to the increase in brittleness of metals with decrease in temperature. [Seok \(2000\)](#) showed that as the ultimate strength increases with decrease in temperature, there is a corresponding reduction in percentage elongation, due to increase in brittleness. A number of engineering SSCs for PS ([Bai et al., 2014](#), [Han et al., 2009](#), [Qiu, 2010](#), [Rudland et al., 2003](#), [Wang et al., 2001](#), [Wilkowski et al., 2008](#)) were analyzed as shown in [Figure 2.2](#). These data were fitted to a linear function allowing us to have a direct relationship between ultimate strength of PS with maximum fracture strain. [Figure 3.3](#) illustrates the linear relationship found. Mathematically the linear relationship can be represented by:

$$\epsilon_f = \frac{P - \sigma_u}{Q}, \quad (3.21)$$

where ϵ_f is the maximum fracture strain and σ_u is the ultimate stress, numerically equal to the stress before necking for PS. P and Q are two constants which are obtained from the linear plot in [Figure 3.3](#). The values of P and Q are found to be 1343 N/mm^2 and 2311 N/mm^2 respectively. It has been previously shown that σ_u can be obtained from [Eq. \(2.1\)](#). This value can be used in the above equation to obtain the fracture strain at any temperature. Ultimately using [Eq. \(3.21\)](#), the maximum true stress at that particular temperature can be obtained using the modified Johnson-Cook model.

3.3 Damage due to void formation

All the above mentioned analytical models for describing stress strain behavior works very well before the necking point. Findings in the field of damage mechanics show that after the necking point when damage of the material begins, there is gradual generation of voids in the material. These ideas were essentially introduced by [Kachanov \(1961\)](#) and later improved by [Rabotnov \(1969\)](#). The voids generated essentially results in increasing the actual stress experienced by the surface. A wide number of researchers reported similar observations ([Gurson, 1977](#), [Kachanov, 1994](#), [Lemaitre, 1985](#)) and many stated that damage occurs as a result of growth and nucleation of voids generated in the structure at damage initiation. This phenomenon can be explained by considering a damage variable D such that the effective stress σ_{eff} can be represented by:

$$\sigma_{eff} = \frac{\sigma_f}{1 - D} \quad (3.22)$$

The damage variable in simple terms can be defined as the ratio of section area covered by voids S_{void} to the nominal section area S_0 . Mathematically,

$$D = \frac{S_{void}}{S_0} \quad (3.23)$$

At room temperature, D can be correlated to another coefficient introduced by [Tvergaard and Needleman \(1984\)](#) known as void volume fraction f . If the total volume is V and the volume occupied by voids is V_{void} , the void volume fraction can be mathematically described as:

$$f = \frac{V_{void}}{V_0} \quad (3.24)$$

We are more interested in the void volume fraction at complete fracture, denoted by f_f . [Tvergaard and Needleman \(1984\)](#), [Becker et al. \(1988\)](#) and many other researchers presented $f_f = 0.25$ for metals at room temperature.

In order to relate the void volume fraction and damage variable, we idealize a simple model of a spherical void, radius of the sphere being r inside a cubical space of side length a . This model is based on the works of [Rice and Tracey \(1969\)](#) and [Gurson \(1977\)](#). The spherical void model is illustrated in [Figure 3.4](#). Thus,

$$V_{void} = \frac{4\pi r^3}{3} \quad \text{and} \quad V = a^3 \quad (3.25)$$

The void volume fraction f can then be mathematically represented by:

$$f = \frac{4\pi r^3}{3a^3} \quad (3.26)$$

In this simplistic model, we use the maximum area of the void to calculate damage variable. This corresponds to the most conservative approach to find the damage variable and is represented by the plane ABCD in [Figure 3.4](#). Thus,

$$S_{void} = \pi r^2 \quad \text{and} \quad S = a^2 \quad (3.27)$$

Similar to f , the damage variable D can be mathematically represented by:

$$D = \frac{\pi r^2}{a^2} \quad (3.28)$$

Using [Eq. \(3.26\)](#) and [Eq. \(3.28\)](#), the void volume fraction and the damage variable can be inter-related. Thus using $f_f = 0.25$ from the literature, we can obtain $D \approx 0.48$ for room temperature.

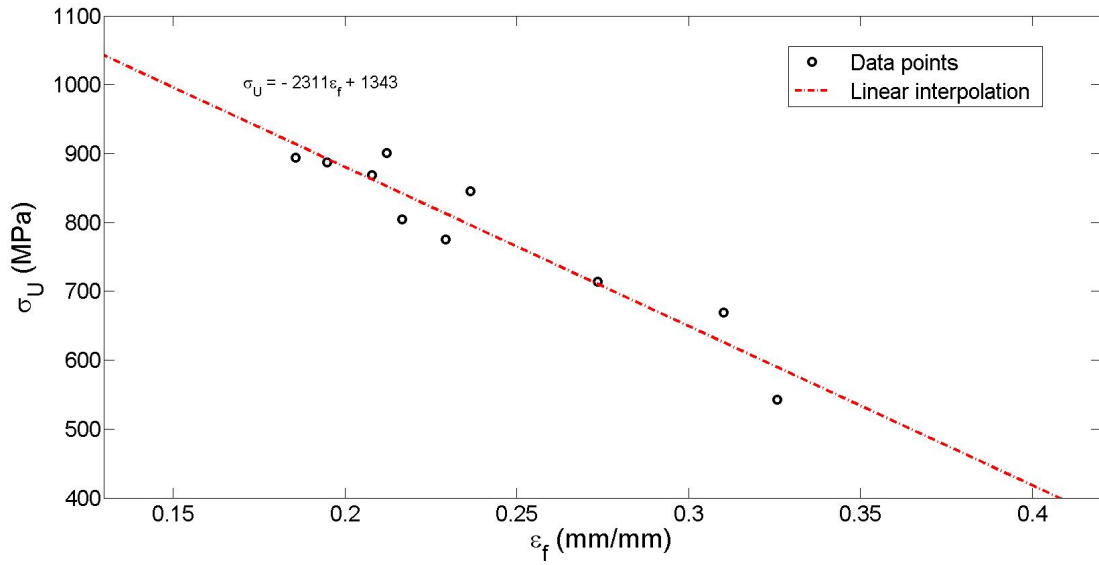


Figure 3.3: Relationship between ultimate stress and maximum fracture strain

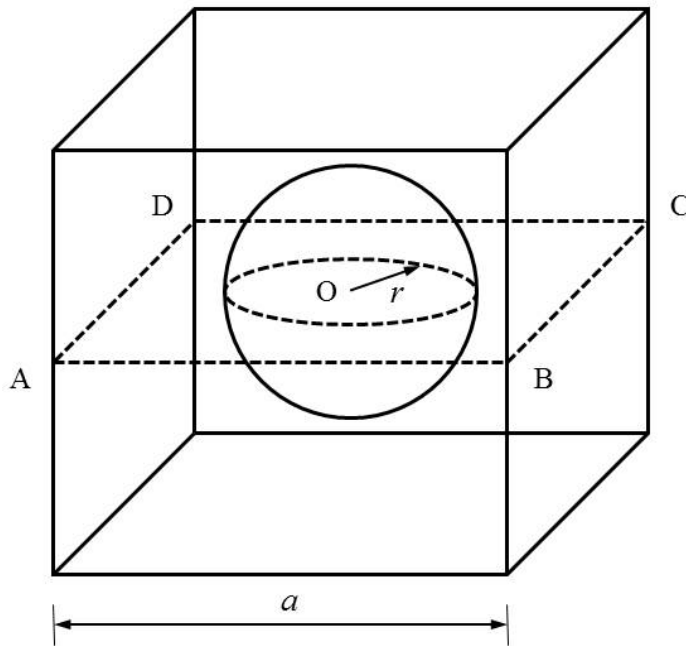


Figure 3.4: Relationship between damage variable D and void volume fraction f

3.3.1 Temperature dependency of damage variable

Damage variable D was conveniently found for room temperature. However, the value of damage variable at complete fracture also varies with temperature (Perez-Bergquist et al., 2014). Due to lack of supporting experimental data for D at other temperatures, the value of the damage variable D at a temperature of 0°C has been found by running the finite element (FE) model several times until a match with the load-displacement curves has been obtained. More details about the validation of the model has been given in Chapter 5.

Table 3.1: Variation of damage variable with temperature obtained from numerical simulations

Temperature, T	Damage variable, D
K ($^\circ\text{C}$)	
298(25)	0.48
273 (0)	0.43

The values of D that has been obtained is well in accordance with other values reported for steel. Lemaitre (1985) reported that $0.2 \leq D \leq 0.8$. The present model complies well with his arguments.

Based on Table 3.1, we can assume a weak linear temperature dependency of damage variable as follows:

$$D = 0.002T - 0.116 \quad (3.29)$$

where T is the temperature in Kelvin scale, p and q are two constants where $p = 0.002K^{-1}$ and $q = 0.016$. This proposed empirical formula for temperature dependency of D can only be valid for a limited range of temperature. Mathematically, the equation

is valid until a minimum temperature of 60K since values for D cannot be negative.

Table 3.2: Mechanical properties of X80 steel used in the FE model

Temperature	Yield strength,	Ultimate strength,	Maximum fracture stress,	Effective maximum fracture stress,
T	σ_y	σ_u	σ_f	σ_{eff}
K (°C)	N/mm^2	N/mm^2	N/mm^2	N/mm^2
323 (50)	530	621	984.91	2095.55
298 (25)	550	646	1003.75	1930.29
273 (0)	570	661	1024.63	1797.60
243 (-30)	588	689	1043.14	1655.78
213 (-60)	605	730	1056.26	1530.81
183 (-90)	620	782	1064.33	1419.11

3.4 Mathematical model for temperature dependency of fracture energy

Fracture energy (or fracture energy per unit area) is a very important toughness parameter that can be essentially defined as the energy required for crack growth in an infinitely large specimen. However, interestingly fracture energy is still considered independent of shape and size of the specimen under study (Bažant and Kazemi, 1990). More details have been explained in Chapter 2. The temperature dependency of fracture energy can be described similar to that illustrated by Figure 2.5. However, there are a few challenges as explained in the following sections.

3.4.1 Ductile to brittle transition

Brittle fracture of numerous Liberty ships during the second World War opened up the world of ductile to brittle transition to the research community. Ductile to brittle transition in metals depend on a number of factors such as specimen geometry, loading rate, loading mode and so on (Capelle et al., 2013). To this end, brittle to ductile transition temperature is not unique for a material, and cannot be considered a material property. The brittle-to-ductile transition temperature for PS has not been reported in the literature very definitively. Toyoda et al. (2012) claims that the transition temperature could be lower than -45°C for PS. Capelle et al. (2013, 2014) reported that the transition temperature for PS (X65 steel) is around -100°C , and positively below -80°C . In the present research, we are more interested in the range of temperatures between which brittle-to-ductile transition occurs.

Rinebolt and Harris (1951) showed that as the carbon percentage for steel decreases, the temperature range over which the brittle-to-ductile transition occurs decreases, and also the transition occurs at a lower temperature. The weight percentage of carbon for X80 is around 0.06-0.08 (Table 2.1). Hence its temperature range for brittle-to-ductile transition should be comparatively smaller. Based on these evidences, we take the interval during which the material experiences a transition from ductile to brittle to be 50°C . Further, in accordance with Capelle et al. (2013, 2014), it is assumed that the brittle-to-ductile transition occurs between -80°C and -130°C .

3.4.2 Upper-shelf and lower-shelf fracture energy

Another challenge in the present problem is to determine the upper shelf fracture energy and the lower shelf fracture energy. The values used here for upper shelf fracture energy, $J_{Ic,d}$ and lower shelf fracture energy $J_{Ic,b}$ have been found out by a thorough literature

survey of fracture toughness parameters for PS (Capelle et al., 2013, 2014, Chao et al., 2007, Fassina et al., 2011, Zhu et al., 2006).

With the above deductions in mind, the assumed temperature dependency of fracture energy can be mathematically expressed as:

$$J_{Ic} = \begin{cases} J_{Ic,b} & : T \leq T_b \\ J_{Ic,b} + J^*(T - T_b) & : T_b < T < T_d \\ J_{Ic,d} & : T \geq T_d \end{cases} \quad (3.30)$$

where T is the working temperature in Kelvin scale, J_{Ic} is the critical fracture energy for each temperature in kJ/m^2 . T_b corresponds to the temperature marking the end of brittle region, T_d corresponds to the temperature where the complete ductile behavior of PS initiates with increase in temperature, $J_{Ic,d}$ is taken as $120 kJ/m^2$, which is approximately equal to the average value of fracture energy or fracture toughness reported by Fassina et al. (2011). $J_{Ic,b}$ is taken as $40 kJ/m^2$, which corresponds to low temperature fracture energy for PS Capelle et al. (2013, 2014). Further J^* is a dimensional constant and is given by $J^* = \frac{J_{Ic,d} - J_{Ic,b}}{T_d - T_b}$. It is numerically equal to $1.6 kJm^{-2}K^{-1}$. The above mentioned linear temperature dependency assumes a very sharp distinction between the three regions of temperature dependency.

In reality, however, there is a more gradual transition between the regions which can be represented by a hyperbolic tangent curve (Capelle et al., 2014). In this regard, an attempt was made to describe the variation of fracture energy with temperature with a single equation as shown below:

$$J_{Ic} = J_{Ic,ref} + (J_{Ic,d} - J_{Ic,ref})\tanh\{E^*(T - T_{ref})\} \quad (3.31)$$

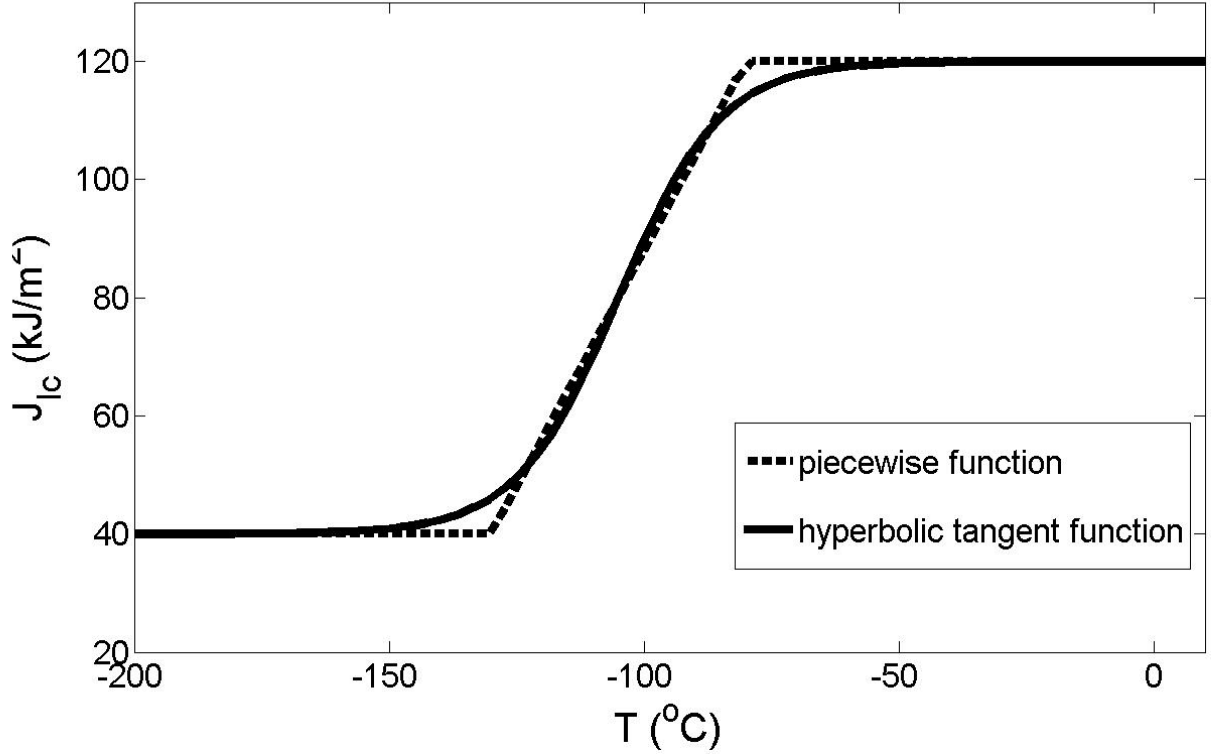


Figure 3.5: Temperature dependency of fracture energy based on Eqs. (3.30) and (3.31)

where $T_{ref} = (T_b + T_d)/2$ is the reference temperature and $J_{Ic,ref}$ is the fracture energy at the reference temperature T_{ref} , which can be obtained from Eq. (3.30). E^* is a constant that is dependent on the upper shelf and lower shelf J_{Ic} values. E^* has been found to be equal to $1/20K^{-1}$. The above equation provides the relationship between J_{Ic} and temperature in all the three regions. A deeper illustration can be obtained from Figure 3.5, which provides the curves for both the cases.

It is worthy to note that in the present model, to capture the temperature effects, the small variation in the fracture toughness in regions I and III are neglected. This assumption is mainly to maintain the simplicity of the model and is in accordance with the results observed by many researchers.

Even though fracture toughness is presented by the fracture energy in the above

arguments, some other toughness parameters like stress intensity factor also follows the same trend and can be represented by a similar equation.

Chapter 4

Temperature dependent cohesive zone model

A cohesive zone can be idealized by assuming two cohesive surface in the direction of crack growth. These two surfaces are held together by cohesive traction or cohesive stress, or simply traction. A cohesive zone fracture model is governed by the cohesive law or traction separation law (TSL) between the cohesive surfaces. Out of a wide number of different forms of TSL as shown in Chapter 2, a linearly-increasing exponentially-decreasing TSL has been chosen for the present problem. This specific traction-separation relationship has been previously verified to produce reliable results for pipeline steel (PS) by [Ren and Ru \(2013\)](#) and [Yu and Ru \(2015\)](#). The details of the TSL is provided in the upcoming sections.

4.1 Mathematical model for traction-separation law

The assumed relationship between traction and separation between the cohesive elements in a cohesive zone model (CZM) is the prime factor which determines the validity

of the model. The traction and separation relationship employed in the present research may be mathematically represented as follows:

$$\boldsymbol{\tau}_0 = (1 - \bar{D})\mathbf{K} \cdot \boldsymbol{\delta} \quad (4.1)$$

where $\boldsymbol{\tau}_0$ is the static traction stress vector, $\boldsymbol{\delta}$ is the separation vector (between the cohesive elements), \mathbf{K} is the elastic stiffness matrix. However for axially running crack with pre-defined crack direction, only the normal components of traction as well as separation are important. Therefore, the three-dimensional traction-separation law can be simplified as follows:

$$\tau_0 = (1 - \bar{D})K \cdot \delta \quad (4.2)$$

where τ is the static traction and δ is the corresponding separation. K is the scalar elastic stiffness \bar{D} is known as the damage scalar. The parameter \bar{D} is different from the damage variable D introduced in the Chapter 3, and can be mathematically represented by:

$$\bar{D} = \begin{cases} 0 & : \delta < \delta_0 \\ 1 - \frac{\delta_0}{\delta} \left[1 - \left(\frac{\delta - \delta_0}{\delta_m - \delta_0} \right)^\alpha \right] & : \delta \geq \delta_0 \end{cases} \quad (4.3)$$

where δ_0 and δ_m are the separation at which damage initiates and complete fracture occurs respectively, and α is an exponent that controls damage evolution. A convex TSL ($\alpha > 1$) can be applied to ductile materials whereas a concave TSL ($0 < \alpha < 1$) is mostly used for CZM of brittle materials (Scheider et al., 2014, Volokh, 2004).

The area under the TSL is known as CZM cohesive energy G and can be defined

as:

$$G = \int_0^{S_m} \tau dS \quad (4.4)$$

Using Eq. (4.2) and Eq. (4.3), G can be found out as:

$$G = \left(1 - \frac{1}{\alpha + 1}\right) K \delta_0 \delta_m + \left(\frac{1}{\alpha + 1} - \frac{1}{2}\right) K \delta_0^2 \quad (4.5)$$

4.2 Temperature effects on traction-separation law

Traction separation law for any material is largely governed by two independent parameters (Cornec et al., 2003, Elices et al., 2002, Park and Paulino, 2013):

1. maximum traction, τ_{max}
2. cohesive energy, G

The effect of temperature on TSL can be illustrated by demonstrating the temperature effects on these individual parameters.

For the TSL described by Eq. (4.2), the parameters δ_0 and δ_m also indirectly influences the validity of the CZM. It is to be noted here that in the present problem, the separation at damage initiation δ_0 and damage completion δ_m have been assumed to remain constant with change of temperature. This assumption is primarily due to lack of evidence of temperature-dependent variation of these parameters. δ_0 was taken equal to 0.025 mm and δ_m was considered equal to four times δ_0 (Ren and Ru, 2013, Yu and Ru, 2015).

4.3 Maximum traction

Cohesive traction is the stress that binds together the two cohesive surfaces. The parameter of interest here is the maximum value of cohesive traction T_{max} . This maximum traction T_{max} is directly related to the elastic stiffness K as shown:

$$K = \frac{T_{max}}{\delta_0} \quad (4.6)$$

The maximum traction for a TSL can be compared to the true stress from uniaxial tensile stress. The maximum traction of TSL between two cohesive surfaces is given by the maximum effective true stress of the material at fracture point (Cornec et al., 2003).

$$T_{max} \simeq \sigma_{eff} \quad (4.7)$$

σ_{eff} can be obtained from the procedure explained in Chapter 3. Thus, for any temperature the value of T_{max} and subsequently K can be easily obtained.

4.4 Cohesive energy and damage evolution

Cohesive energy G is equal to the area under the TSL (Chanda and Ru, 2015a,b) and is given by Eq. (4.5) for the present problem. Cohesive energy is equal to the work done to create a new surface due to crack growth, and is equal to fracture energy per unit area or fracture toughness (Park and Paulino, 2013).

$$G \simeq J_{Ic} \quad (4.8)$$

Thus by obtaining the value of J_{Ic} from Eq. (3.31) for any temperature, the cohesive energy can also be obtained at that particular temperature. Using Eq. (4.5), the corresponding value of α can be obtained. Thus, all the parameters of the TSL to be used for modeling dynamic fracture of PS can now be obtained for any particular temperature.

4.5 Effect of dynamic crack growth

Until now, the entire formulation was done based on static traction. However, to account for the dynamic crack growth in PS, the dependency of traction on dynamic parameters needs to be considered. The dynamic traction τ can be related to the static traction τ_0 according to the following relation:

$$\tau = k_d \tau_0 \quad (4.9)$$

where k_d is the parameter to convert the static TSL model to a dynamic one. The effect of dynamic crack growth has been captured by the parameter k_d . Ideally, [Yu and Ru \(2015\)](#) has presented that k_d follows the following model:

$$k_d = 1 + \eta \left(\frac{\dot{\delta}}{\dot{\delta}_r} \right)^\beta \quad (4.10)$$

Here, $\dot{\delta}$ is the separation rate and $\dot{\delta}_r$ is the reference separation rate. The constants η and β need to be determined from test results. In accordance with [Yu and Ru \(2015\)](#), $\dot{\delta}_r$ has been taken as 1 m/s, η has been taken equal to 4×10^{-3} and β has been taken 2 for the calculation of k_d . For the current problem, the numerical value of k_d does not vary a lot. It stays between 1.03-1.28 throughout the fracture process at any temperature. These small variations do not implement a huge variation in the fracture

process. Thus, to reduce computational complexity, an average value of k_d has been implemented. Table 4.1 provides numerical values of separation rate and corresponding k_d for a temperature of -30°C . Based on the observed values, k_d has been assumed to be a constant at any temperature in the present problem and equal to 1.1 for all cases.

Table 4.1: Example of separation rate and corresponding k_d at steady-state for the FE simulation at a temperature of -30°C

Time	Separation rate	Parameter
<i>ms</i>	<i>m/s</i>	k_d
0.4	5.14	1.106
0.6	4.99	1.099
0.8	4.78	1.091
1.0	4.36	1.076
1.2	4.41	1.078
1.4	4.19	1.070

Figure 4.1 graphically illustrates the final TSL at different temperatures as implemented in the finite element simulations.

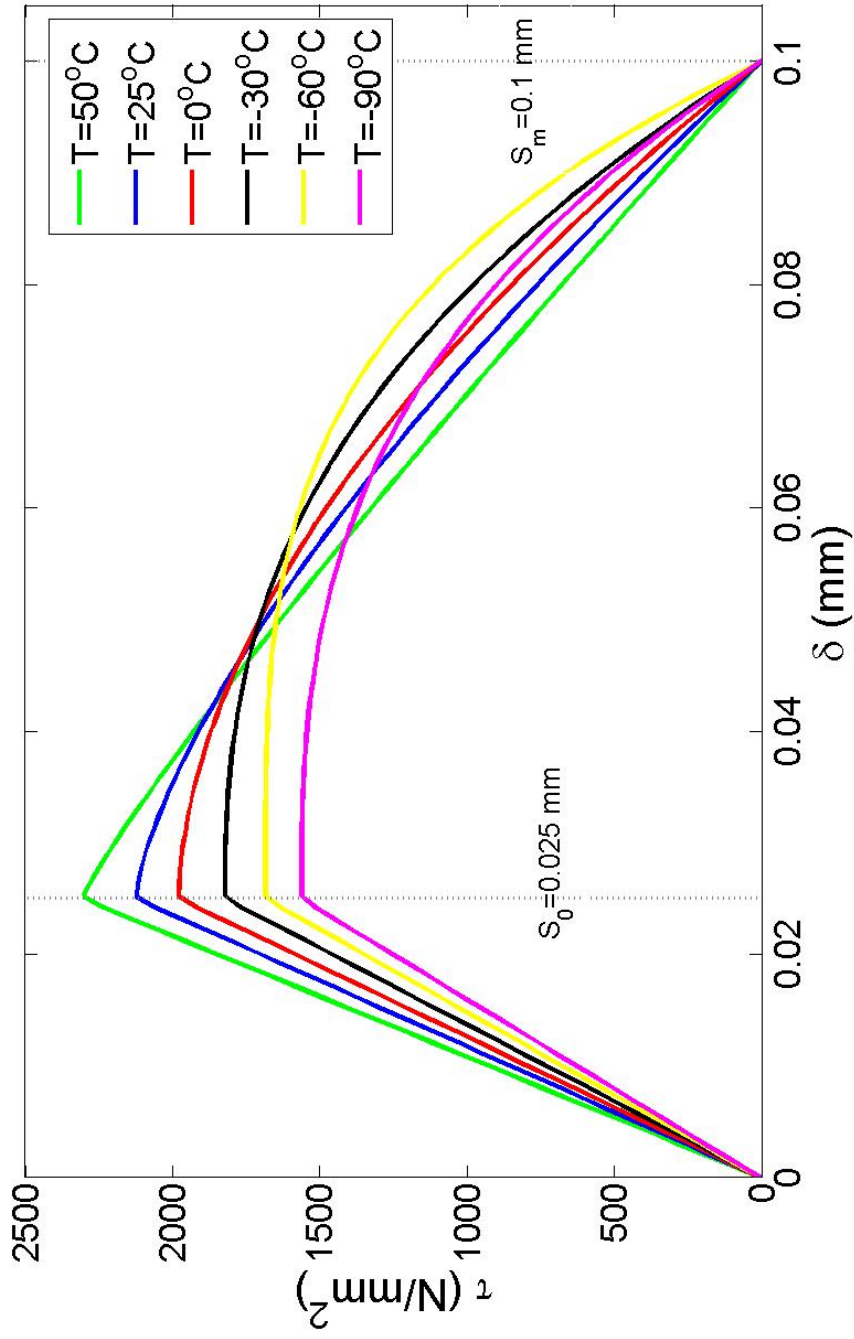


Figure 4.1: Traction-separation relationships between the cohesive surfaces for six different temperatures

Chapter 5

Temperature dependent CZM-based finite element model

The temperature dependent cohesive zone model (CZM) has been explained in the previous chapter in detail. The CZM has been implemented through a finite element (FE) modeling of Drop Weight Tear Test (DWTT) using Abaqus/CAE 6.13. Before providing an elaborate description of the temperature dependent FE model, it is important to provide a brief review of existing FE models for pipeline steel (PS).

5.1 Temperature independent FE models

A wide number of temperature independent FE model to simulate DWTT can be found in the literature (Marotta et al., 2012, Minotti and Salvini, 2011, Parmar, 2014, Scheider et al., 2014, Wu et al., 2013). For PS, the most recent FE models have been reported by Ren and Ru (2013) and Yu and Ru (2015). Ren and Ru (2013) performed a strain-rate independent analysis where the TSL was modified to match the numerically obtained load displacement curves with those obtained from experiments. The primary

goal of the research was to generate a numerical method to simulate dynamic fracture growth of PS, and thus significantly reduce the complexity of the experiments and the associated high costs. [Yu and Ru \(2015\)](#) improved on the previous model by using a strain-rate dependent model. They argued that the strain rate dependency of the model does play an important role in determining the dynamic fracture behavior of PS. The most vital inclusion by [Yu and Ru \(2015\)](#) was the use of user sub-routine VUMAT to model the cohesive elements in the CZM based FE model. In other words, the TSL used were rate dependent and it was implemented based on the separation rate of the crack tip. However, in both these models, there was no real physical justification about the assumed TSL. The TSL was obtained on a trail and error basis to match up with test results. Thus these previous results could be used for just one special case and could not be generalized so that the FE model could be used for different operating conditions. The present research primarily works in this area and tries to overcome this shortfall by obtained the CZM parameters from correlation with known mechanical behavior of PS. This procedure has been elaborately explained in [Chapter 4](#).

5.2 Temperature-dependent FE model

The present FE model is an improvement on [Ren and Ru \(2013\)](#) and [Yu and Ru \(2015\)](#) FE models. These models have not considered the temperature dependency of TSL. Further there was not much reason behind the assumed values of CZM parameters.

The FE model for PS has been made according to the test procedure of Drop Weight Tear Test (DWTT) that is widely used for fracture analysis of steel and for measuring fracture toughness. [Figure 5.1](#) shows the test setup for DWTT as implemented in the present problem.

One primary prerequisite of a FE model is that the crack growth direction needs to be pre-defined. Once the crack growth direction is known, the specimen is modeled in two parts. The two cohesive surfaces are defined separately, and bound together by the TSL. The traction separation relationship governs the behavior of the cohesive surfaces of the FE model. It is to be noted here that the two supports in DWTT were modeled as perfectly rigid in the ABAQUS simulations.

5.2.1 Specifications of DWTT

DWTT has been explained in Chapter 2. Here the dimensions, weight and other details of the apparatus required for the test will be specified. The details used in the simulations is according to the DWTT performed and reported by Shim et al. (2010). The mass of the hammer was considered to 780.19 *kg* and the impact velocity of the hammer during operation was 7.53 *m/s*. A standard DWTT specimen was used for the FE model. The length and height of the specimen are 304 *mm* and 76.2 *mm* respectively. The V-notch angle in the specimen is 45° and had a vertical length of 5 *mm*. The thickness of the specimen is 12 *mm*.

5.2.2 Meshing of the model

Meshing of the model has been done using a mapped meshing procedure. Finer mesh has been used near the crack tip. The mesh size of the elements near the crack tip and along the crack propagation direction has been reduced to 0.145 *mm* × 0.148 *mm* × 0.375 *mm* for better accuracy of the results. Since the direction of crack growth is pre-determined, there was no need for remeshing in Abaqus/CAE for creating this FE model.

Two different types of solid 3D elements were used to generate the FE model, the

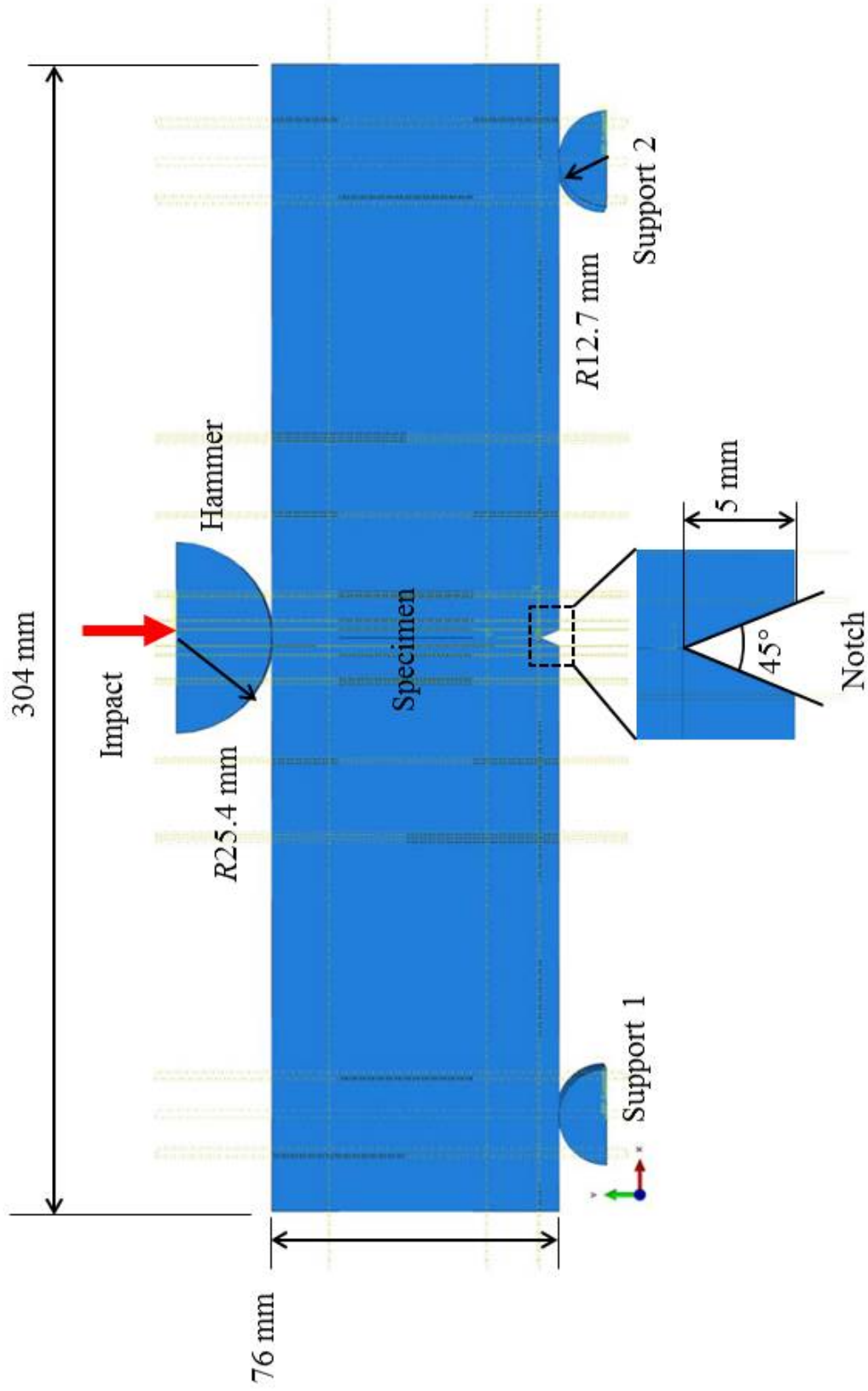


Figure 5.1: Specifications of DWTT used in the FE model

total number of elements being 322690. Out of them, 52666 are linear wedge elements of type C3D6 and the rest 270024 are linear hexahedral elements of type C3D8R. The total number of nodes used in the model are 334246. Table 5.1 gives the details of meshing for the individual parts of the model. Another interesting feature of the present model is that cohesive surfaces, and not cohesive elements have been used to model the CZM along crack growth direction. This added simplicity to the model and unnecessary clutter of the mesh with a varied number of different elements was avoided.

Table 5.1: Details of meshing for individual instances

Instance name	Total elements	Type C3D6	Type C3D8R	Total nodes
Specimen (left)	160274	25262	135012	166275
Specimen (right)	160274	25262	135012	166275
Hammer	1014	1014	0	776
Left support	564	564	0	460
Right support	564	564	0	460

5.3 Verification of the present model

The FE model described in the previous sections have been compared with the test results from Shim et al. (2010). According to normal convention, the comparison has been done based on the load-displacement curves for X80 steel. The contact loading and the corresponding displacement for the specimen under study has been obtained for two different temperatures for validation. Figure 5.4 shows the FEA results and test results (Shim et al., 2010) for room temperature. There seems to be a quite good match of the FEA results with test results from the literature. The location of the pop-in (Anderson, 2005) in the load-displacement curve has also been quite accurately

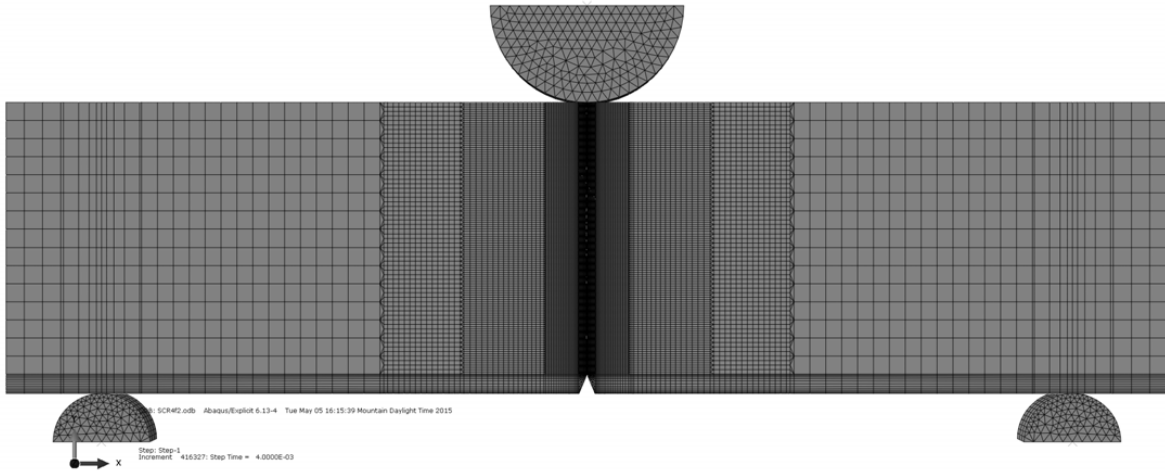


Figure 5.2: Illustration of meshing of the FE model

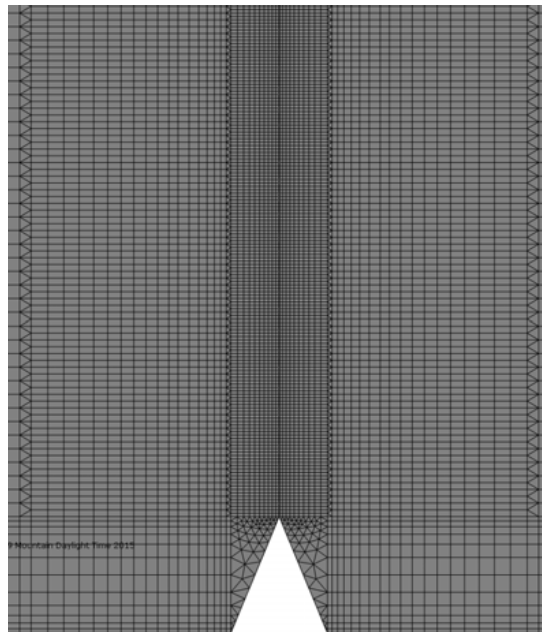


Figure 5.3: Finer mesh near the crack tip for accuracy of numerical analysis

predicted by the FEA. The minor deviations mainly in the elastic zone of the curve before damage initiation can be neglected since it is of greater interest to us to study the crack growth in the present problem. The maximum deviation of FE results from test results is approximately 13.8%.

The FE results has also been matched with load-displacement curve from actual DWTT at a temperature of 0°C, which is shown in Figure 5.5. As explained earlier, the match with load-displacement curve for this temperature has been obtained by varying the damage variable D introduced in Chapter 3. Here too we see a quite good match between FEA and experiments. The maximum deviation of FE results from test results in this case is 11.5%.

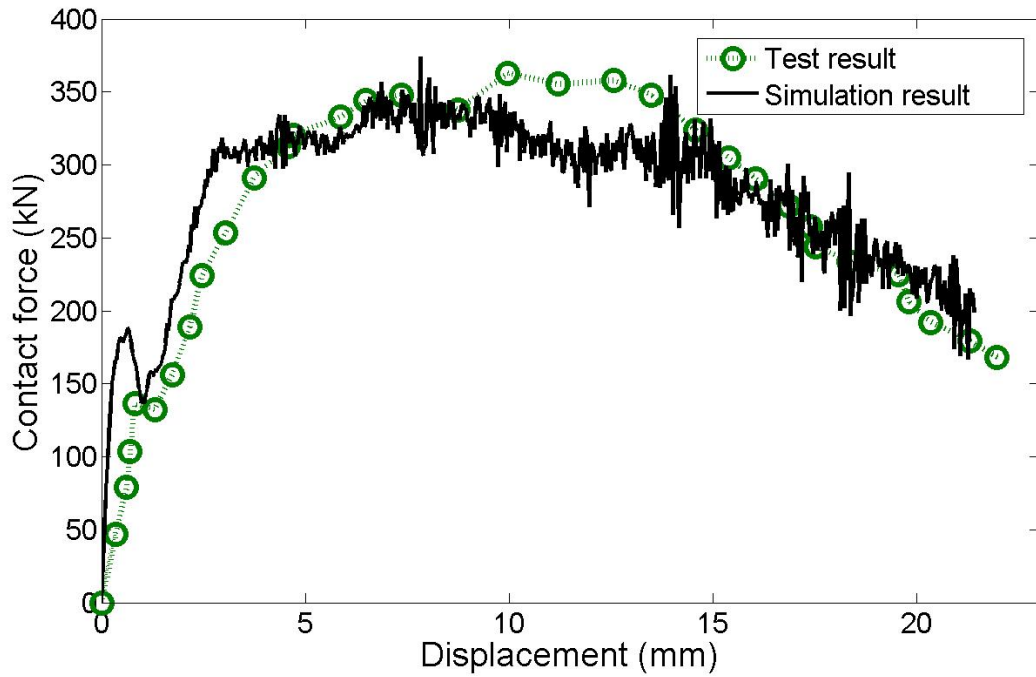


Figure 5.4: Validation: Test results (Shim et al., 2010) and simulation results for X80 steel at room temperature (25°C)

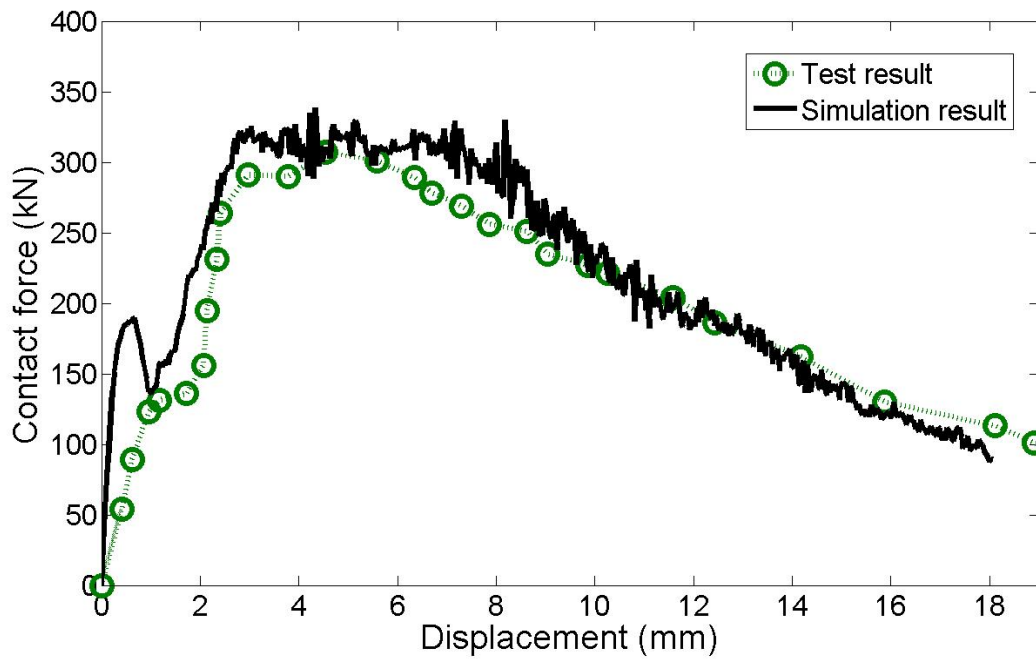


Figure 5.5: Validation: Test results (Shim et al., 2010) and simulation results for X80 steel at a temperature of 0°C

Chapter 6

Temperature dependence of dynamic fracture of pipeline steel

Based on the finite element (FE) model introduced in Chapter 5, a detailed fracture analysis of X80 steel was done. The fracture analysis was done mainly to analyze the various fracture parameters such as CTOA, CTOD, crack length and crack speed. The following sections provide a detailed account.

6.1 Temperature effect on load displacement curve

A load-displacement curve gives us the relation between the contact force or load on the specimen and the resultant displacement of the specimen. Load displacement curves form the basis of validation of a FE model when compared with test results. Figure 6.1 shows the load-displacement curves obtained from the FE simulations for all the six different temperatures. An interesting observation from the figure is that the initial elastic part of the curve before initiation of damage remains similar even when the temperature changes. However, a huge difference can be noticed in the curves once

damage initiates.

Area under the load-displacement curve is equal to the total input energy required for complete fracture of the specimen. Figure 6.1 shows that as the temperature decreases, the total input energy decreases at a significant rate. Since it is difficult as well as computationally expensive to obtain the total area under the curve, another important parameter known as the steady state energy is used for the quantitative analysis (Shim et al., 2010). During steady state crack propagation, the speed of crack growth or the slope of the load-displacement curve remains fairly constant. Figure 6.2 illustrates the steady state crack propagation and approximate steady state energy obtained from the load displacement curves. Table 6.1 gives the values of maximum contact force (or maximum load) and the steady state energy (or steady state energy per unit newly formed crack area) for each temperature of study.

Table 6.1: Maximum load and steady state energy for the load displacement curves at different temperature

Temperature, T	Maximum load	Steady state energy
K ($^{\circ}$ C)	kN	kJ/m^2
323(50)	388	–
298(25)	340	15074
273 (0)	318	12241
243(-30)	326	5981
213(-60)	330	3431
183(-90)	318	1380

The analysis of the load-displacement curve allows us decide whether the fracture process is ductile or brittle. As can be seen from Figure 6.1, brittle fracture is seen for a temperature of -90° C. Other temperatures show ductile fracture, however the ductility

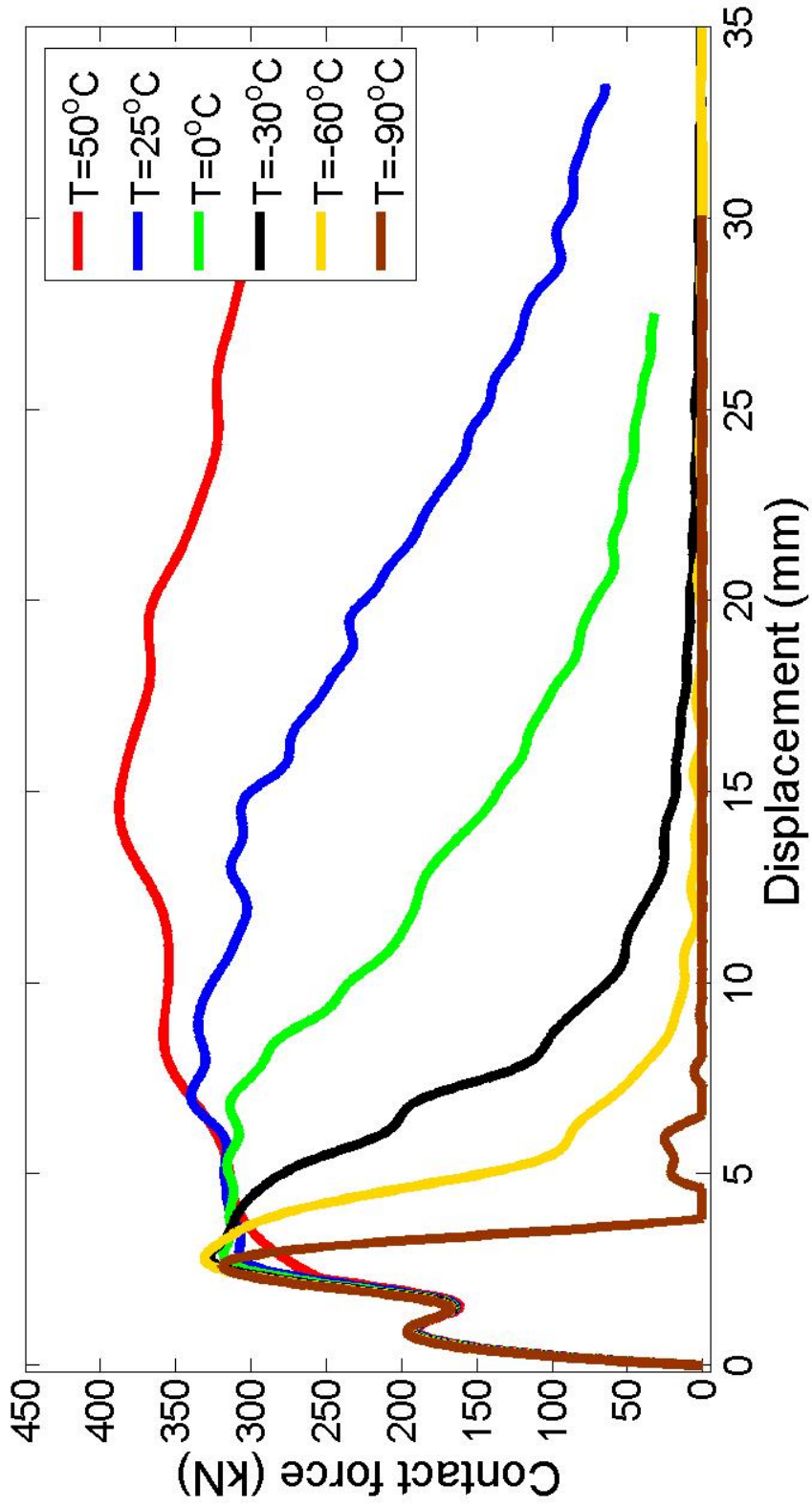


Figure 6.1: Load displacement curves for six different temperatures

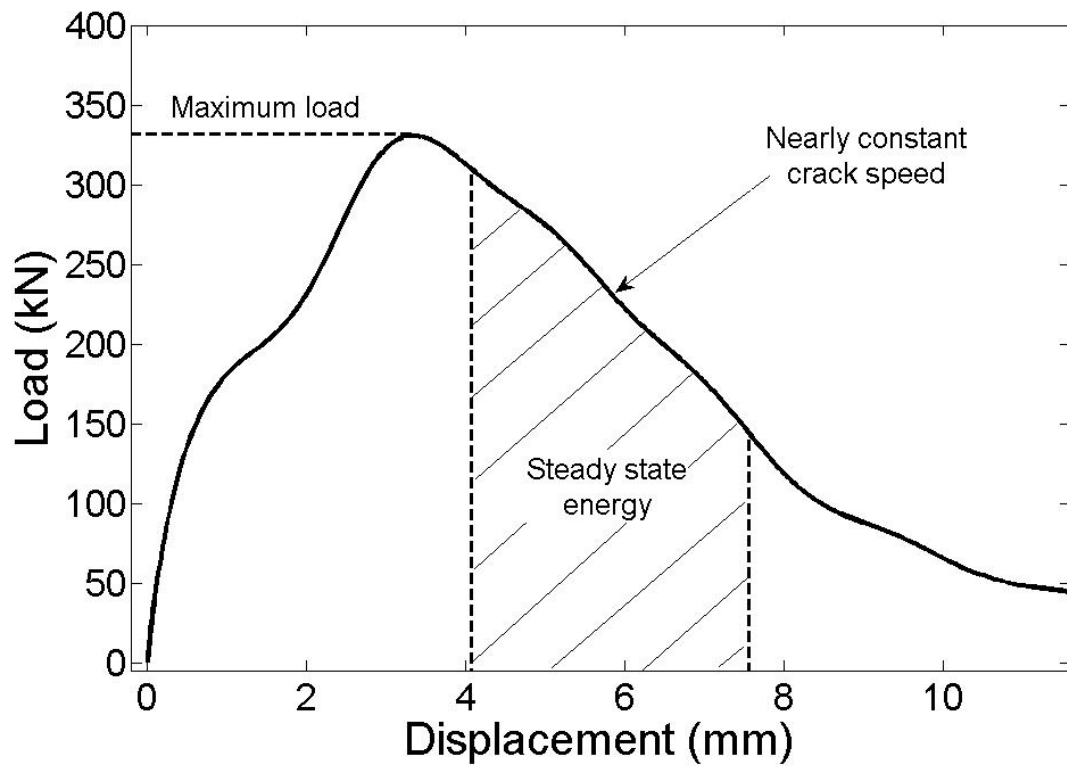


Figure 6.2: Illustration of steady state energy and maximum load on the DWTT specimen through a smoothed load-displacement curve obtained from a FE simulation at a temperature of -30°C .

of the fracture process increases as the temperature increases. This phenomenon can also be interpreted from the increasing trend of the steady state energy with increase in temperature.

6.2 Temperature effect on crack length and crack speed

Crack length is defined as the length of the propagated crack starting from the point of crack initiation whereas the velocity of crack growth in the direction of crack propagation is known as crack speed. Crack speed is numerically equal to the slope of the crack length vs. time curve at any point.

Both crack length and crack velocity can be found out from the time history of the location of the crack tip with respect to a fixed point. In the present model, the crack length at any time has been found out by subtracting the length of the ligament at that particular time from the initial ligament length before crack growth. The crack speed has been obtained from the slope of the crack length vs. time plot for each temperature.

The crack length vs. time plots have been represented in two figures for better illustration. Figure 6.3 shows the crack length for three different temperatures ($T \geq 0^\circ C$). Figure 6.4 shows the crack length for the other three different temperatures ($T < 0^\circ C$).

From the figures, it could be said that steady crack growth occurs from 12 *mm* to 48 *mm* roughly for all temperatures. The crack takes a length of 12 *mm* to achieve steady crack growth. After a crack length of 48 *mm*, a number of other processes like bending become significant which ceases the steady-state crack growth. This in turn is because the ligament length becomes less than 23 *mm* and the steady crack

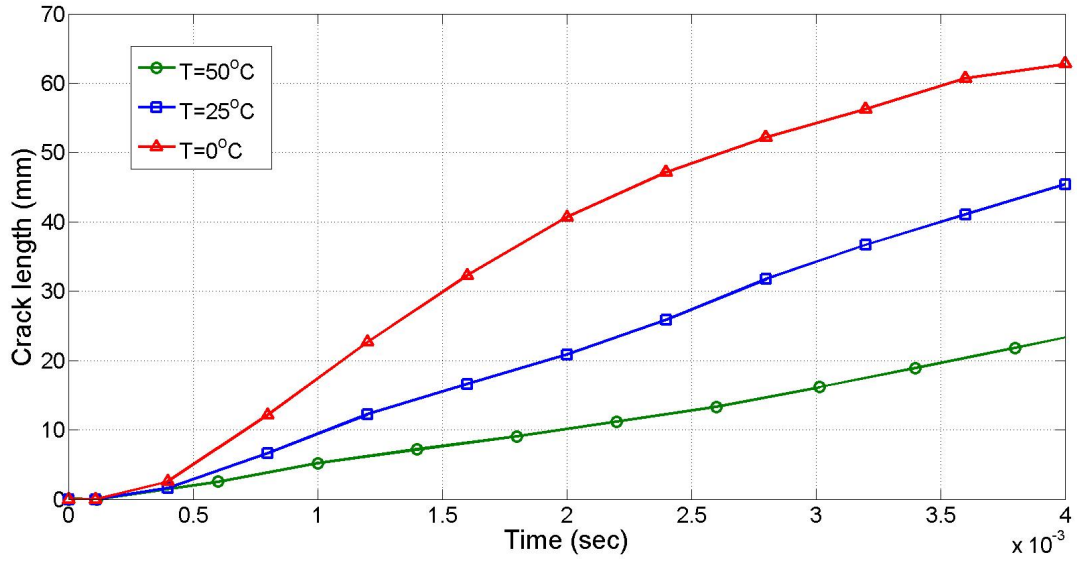


Figure 6.3: Crack length vs. time ($T \geq 0^\circ\text{C}$)

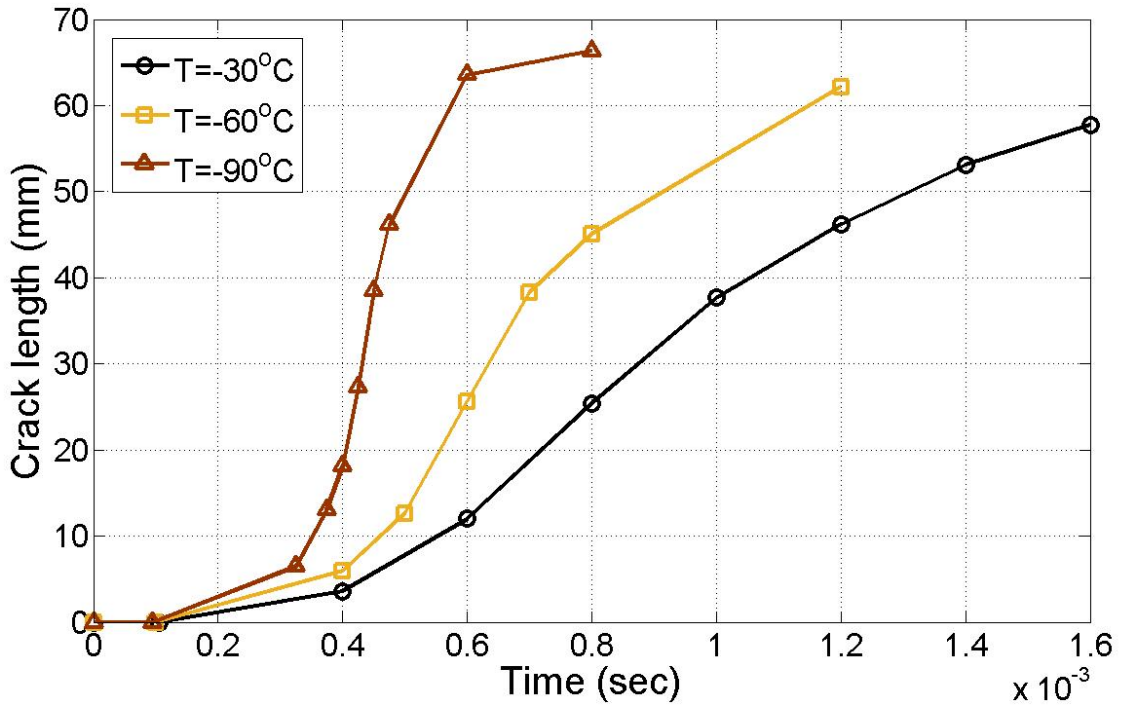


Figure 6.4: Crack length vs. time ($T < 0^\circ\text{C}$)

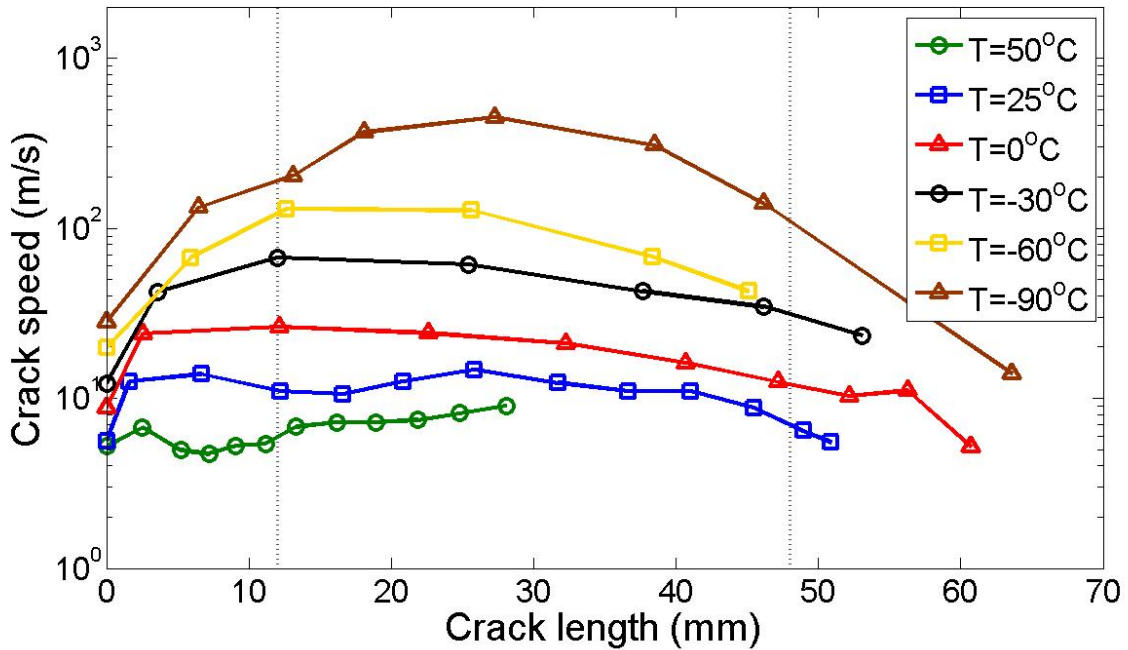


Figure 6.5: Variation of crack speed with crack length

growth with almost constant speed experiences a deceleration. This observation in the present FE model is in accordance with the experimental observations of [Shim et al. \(2010\)](#) where they observed that the last one-third of the initial ligament length of the specimen does not contribute to the steady state crack growth.

Figure 6.5 is a semi-logarithmic plot that shows us the speed of crack propagation with respect to crack length.

6.3 Temperature effect on CTOA

The most widely accepted definition of CTOA or crack tip opening angle states that CTOA is equal to the angle formed by the two newly generated crack surfaces at a distance of 1 *mm* from the crack tip. The early experimental and numerical work by researchers ([Kanninen et al., 1979](#), [Newman, 1984](#), [Yuan and Brocks, 1991](#)) shows

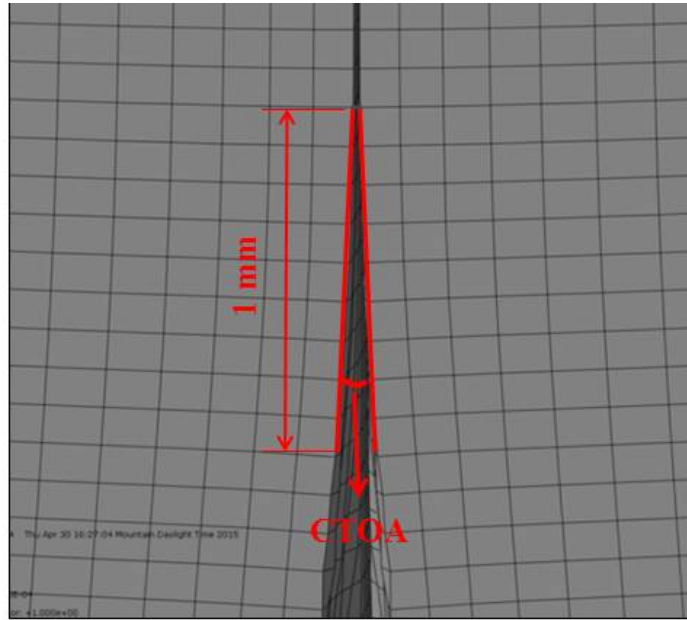


Figure 6.6: Measurement of CTOA

that during steady state crack growth, CTOA reaches a steady state condition. In other words, this suggests that in the steady state crack propagation, CTOA remains fairly constant. Due to this observation, CTOA is presently regarded as a toughness parameter for characterization and differentiation of fracture behavior of different elements. In spite of the fact that CTOA is considered a material parameter, CTOA has been found to be sensitive to changes in fracture speed as shown by [Ren and Ru \(2013\)](#). In the present section, we will analyze the variation of steady state CTOA with temperature from FE simulations.

In the present FE model, CTOA has been measured at a distance of 1 *mm* from the crack tip. The crack tip has been identified as the point when damage starts to initiate and separation reaches a value equal to δ_0 . A three point angle measurement technique has been employed. Figure 6.6 illustrates the measurement technique of CTOA in detail.

The variation of CTOA with crack length has been shown in two different figures

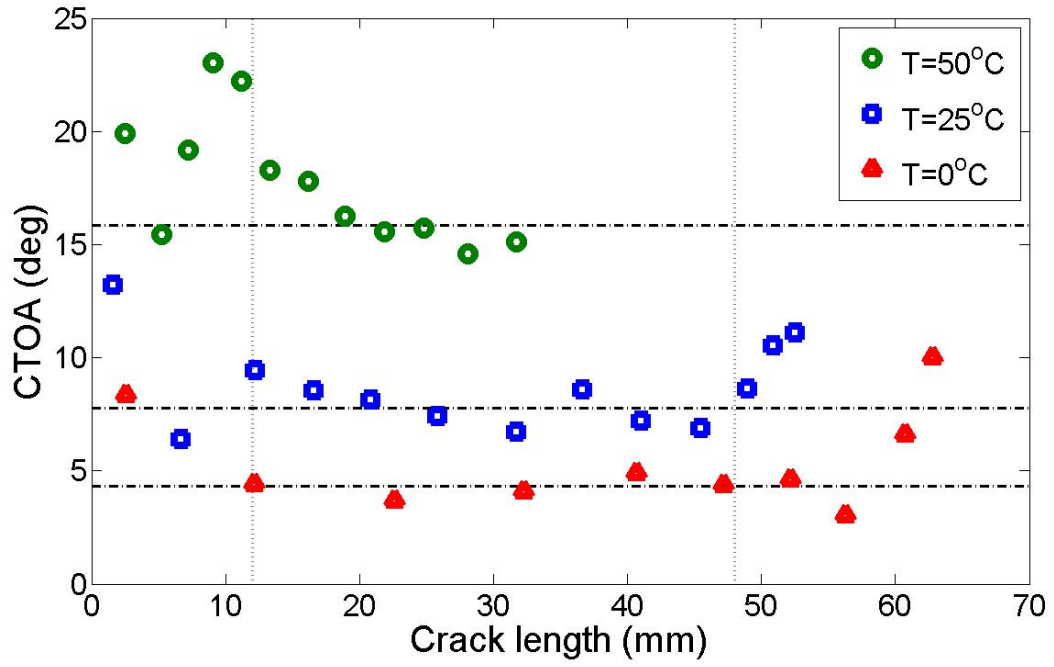


Figure 6.7: CTOA vs. crack length ($T \geq 0^{\circ}\text{C}$)

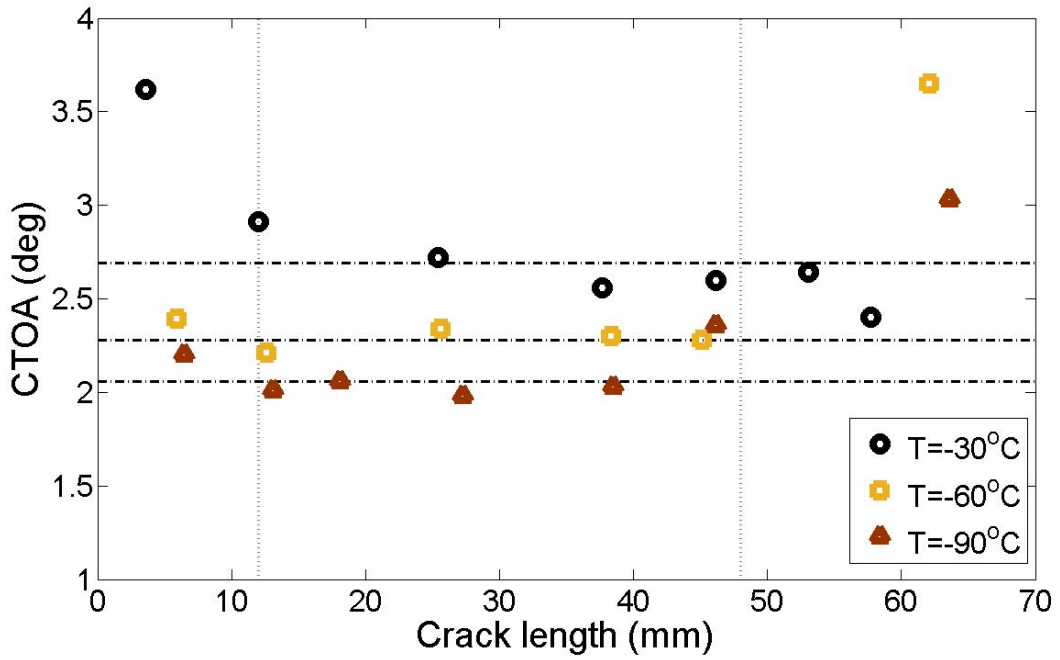


Figure 6.8: CTOA vs. crack length ($T < 0^{\circ}\text{C}$)

for a better explanation and understanding. Figure 6.7 shows the plots for ($T \geq 0^\circ\text{C}$) whereas figure 6.8 shows the plots for ($T < 0^\circ\text{C}$). It is seen that the steady state CTOA value shows a strong exponential dependence on temperature. For temperature less than -30°C , the CTOA values change very little and tend towards a constant value. However, as the temperature increases, the CTOA values increase exponentially. Table 6.2 provides the average CTOA values calculated for all the temperatures.

In the early states of crack propagation, non-constant CTOA values were observed. This observation was similar to Lam et al. (2005) and Newman et al. (2003) which was identified to occur mainly due to initial unstable and unsteady crack growth, and crack tunneling.

6.4 Temperature effect on CTOD

Similar to other fracture toughness parameters, crack tip opening displacement (CTOD) measures the resistance of a material to the propagation of a crack.

The basic idea behind CTOD is a characteristic displacement at the crack tip that controls initiation of a crack as well as stable and unstable crack growth. The appropriate mathematical definition of CTOD is sometimes controversial and different definitions are used for various applications. The two most common measurement technique for CTOD are as follows:

1. displacement at original crack tip (at a fixed distance).
2. displacement at 90° intercept.

In the present finite element models with sharp cracks, the first method has been employed. CTOA is measured at a fixed distance from the crack tip to maintain uniformity of results. In the current model this fixed distance was taken as 1 mm (Amstutz et al., 1997, Lam et al., 2005).

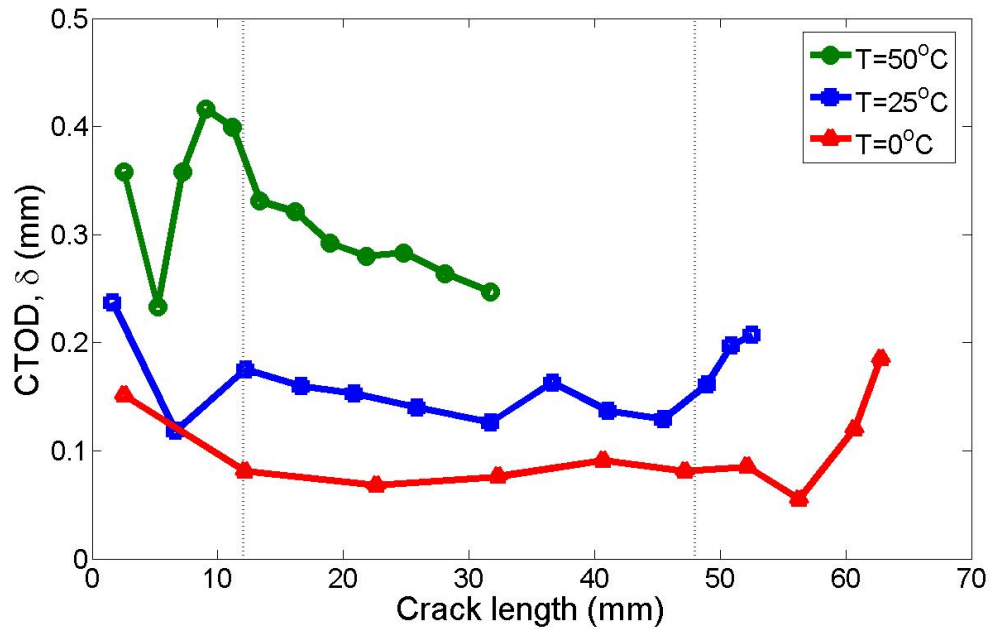


Figure 6.9: CTOD vs. crack length ($T \geq 0^\circ\text{C}$)

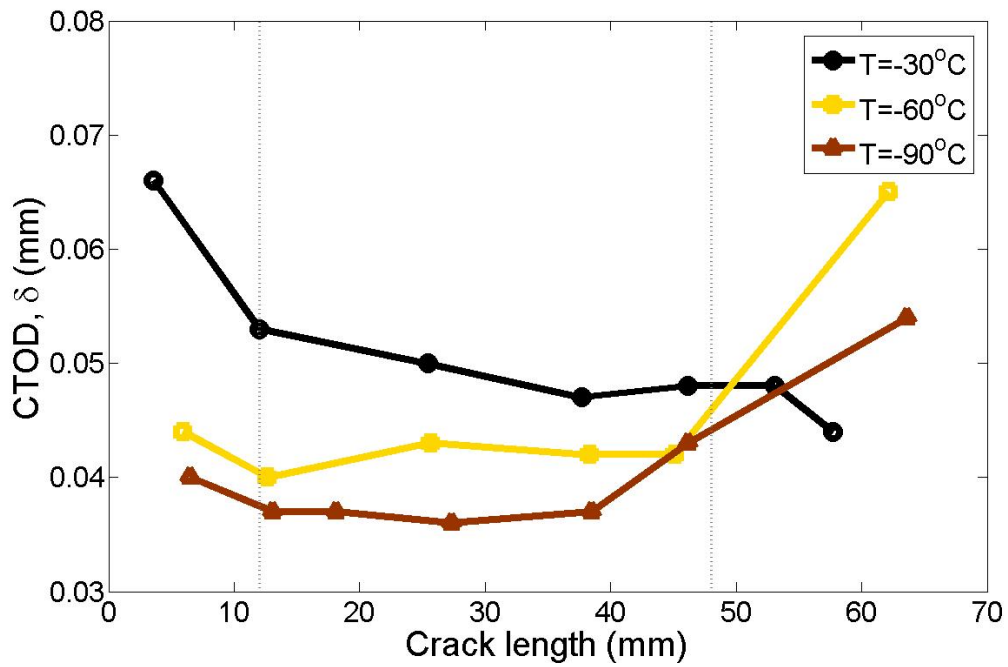


Figure 6.10: CTOD vs. crack length ($T < 0^\circ\text{C}$)

Figures 6.9 and 6.10 shows the plots of CTOD with crack length for all the six different cases of FE simulations. Similar to CTOA, the steady-state values of CTOD has also been obtained and it shows the same trend as CTOA. Table 6.2 provides the numerical values of the steady state CTOD for different temperatures.

6.5 Temperature dependency of toughness parameters

Table 6.2: Average steady state CTOA and CTOD at different temperature

Temperature, T	CTOA	CTOD
K (°C)	°(degree)	mm
323(50)	15.84	0.302
298(25)	7.86	0.146
273 (0)	4.34	0.080
243(-30)	2.69	0.048
213(-60)	2.28	0.042
183(-90)	2.06	0.038

Based on the steady state values of the toughness parameters shown in Table 6.2, an exponential relation can be formulated to account for the temperature dependency of these toughness parameters (CTOA/CTOD) during steady crack growth:

$$\Gamma = (\Gamma_{room} - \Gamma_{\infty})exp(K_1T^*) + \Gamma_{\infty} \quad (6.1)$$

where Γ represents the value of the toughness parameter during steady-state crack growth at a non-dimensional temperature of T^* (defined previously in Chapter 3). Γ_{room} is the value of the toughness parameter at room temperature and Γ_{∞} is the assumed value as T tends to zero in absolute scale. K_1 is a non-dimensional constant which determines the temperature sensitivity of the material with regard to these fracture toughness parameters. For PS, it was found that $K_1 = 43$. Figures 6.11 and 6.12 illustrate the curve fitting for CTOA and CTOD respectively. In both figures, the solid black line represents the prediction by Eq. (6.1).

Table 6.3: Representative values of the toughness parameters for Eq. (6.1)

	$\Gamma = \text{CTOA}$	$\Gamma = \text{CTOD}$
Γ_{room}	7.86°	0.146 mm
Γ_{∞}	2.0°	0.038 mm

Similar results for CTOD for steel specimens were observed by other researchers in three-point bending experiments. The results show the same trend of variation of CTOD with temperature. Ebrahimi and Seo (1996) reported an exponential rise of CTOD values for A543 steel. Similar results were also reported by Sorem et al. (1991) for A36 steel. The similarity with experimental results confirms that our FE model gives reliable prediction of toughness values for PS.

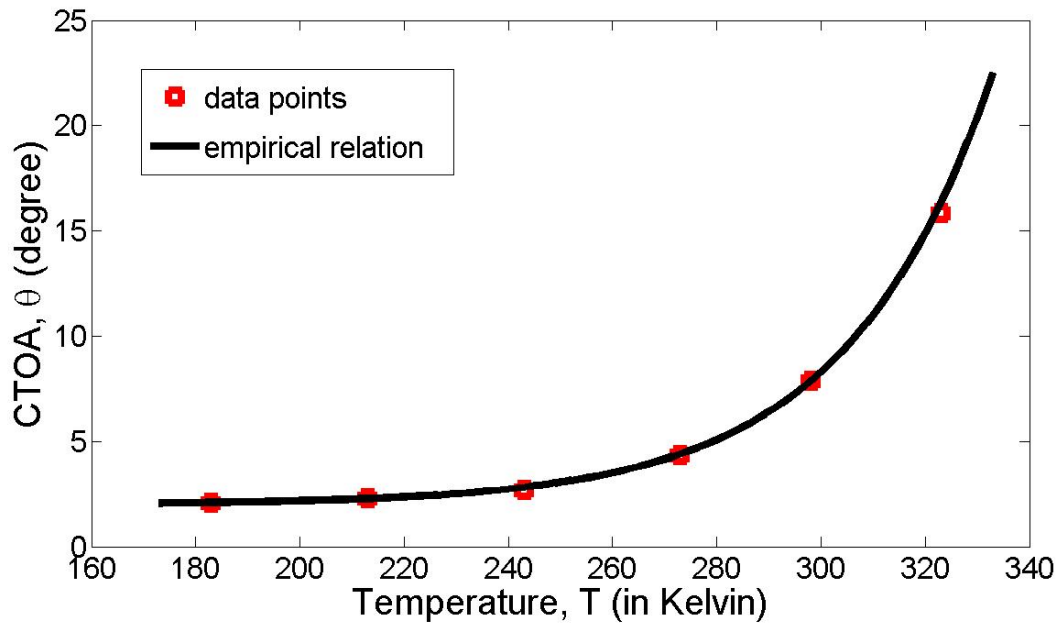


Figure 6.11: Empirical relation for temperature dependency of steady state CTOA

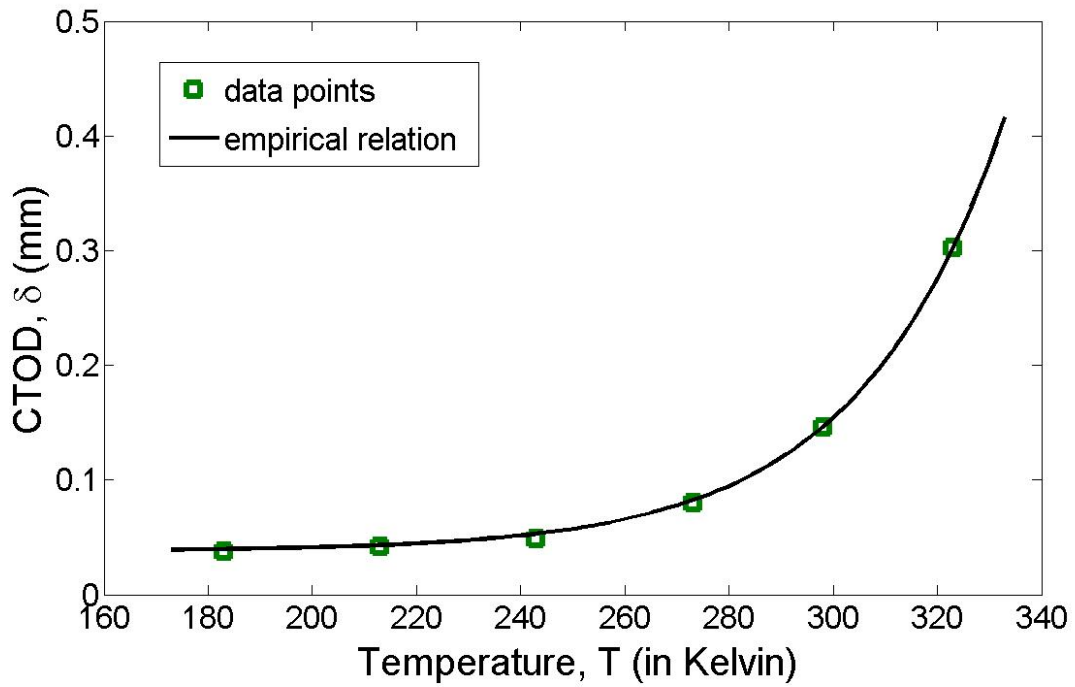


Figure 6.12: Empirical relation for temperature dependency of steady state CTOD

Chapter 7

Summary and Future Work

7.1 Summary of the thesis

The present work reports a cohesive zone model (CZM) for a detailed fracture analysis of pipeline steel (PS) for a wide range of temperatures. The implementation of the CZM has been achieved through a finite element (FE) model made in a commercially available software Abaqus/CAE 6.13. The driving force behind the present analysis was to better understand the temperature dependent fracture behavior of PS. The ultimate motive of the research is to improve the design and manufacturing process of pipelines to minimize rupture of pipelines due to fracture.

This research identifies and quantifies the variation of the essential CZM parameters with temperature. The two essential CZM parameters that define the traction separation law (TSL) are maximum cohesive traction and cohesive energy. The maximum traction is equal to the maximum true stress of the PS under consideration whereas the cohesive energy can be equated to the fracture energy (or fracture energy per unit area) of the material. A temperature dependent relation of maximum true stress and fracture energy has been obtained to define the temperature-dependent CZM.

The FE model of the above CZM was made to simulate a Drop Weight Tear Test (DWTT). Validation of the model was done based on comparison of the load-displacement curve of the present model with that of test results.

Based on the FE simulation for different temperatures, a detailed fracture analysis for PS has been done. The plots of contact force against displacement for different temperatures show a sharp decrease in the amount of steady-state energy required for complete fracture of the specimen when the temperature is decreased. The evolution of crack with time has been plotted. This time history of crack growth identifies a steady-state crack propagation zone where toughness parameters remain almost constant.

Temperature variation of toughness parameters like CTOA and CTOD have been reported. Both CTOA and CTOD show an exponential increase with increase in temperature. This result is consistent with temperature dependent variation of CTOD reported in the literature for steel. This exponential relationship with temperature has been formulated using a simple empirical relation.

The present research provides us the tool to obtain an approximate fracture behavior at any temperature. This will enable designers to be aware of any unwanted scenario that might be experienced in the temperature range of operation of the pipeline. Knowing the fracture behavior of pipelines in the operating range of temperatures can help designers build a long-lasting and trustworthy pipeline in regions experiencing extremes of temperature.

With minor modifications, the temperature dependent CZM proposed here can be implemented for other materials which shows similar characteristics. In short, the present thesis reports a simple but robust CZM-based FE model that can analyze the fracture behavior of PS at different temperatures.

7.2 Future Work

Even though the present work studies the temperature dependence of dynamic fracture through a simple model, a number of improvements can be brought in the present work:

1. In the present model, the effect of strain rate on the TSL have been approximated to maintain the simplicity of the model. However a more accurate model can be obtained by an iterative strain-rate dependent model where the TSL is automatically updated according to the varying strain rate of the model, instead of assuming an average value.
2. The approach presently used to find the maximum traction consists of a number of steps and interferes with a simplicity of the model. Even though the model achieves good match with test results, there is a scope of simplification of the procedure of obtaining maximum traction to ensure ease of operation.
3. The CZM parameters δ_0 and δ_m have been assumed to be constant in the present research. The effects of temperature changes on these parameters could be explored for a more holistic and complete model.
4. In the present model, the effect of changing DWTT hammer speed on temperature dependent fracture has not been analyzed and this might be an area where more research explorations are possible.

Bibliography

- Odd M Akselsen, Erling Østby, and Bård Nyhus. Low Temperature Fracture Toughness of X80 Girth Welds. In *Proceedings of the 22th International Offshore and Polar Engineering Conference*, volume 4, pages 283–289, Rhodes, Greece, 2012.
- Bryon E. Amstutz, Michael A. Sutton, David S. Dawicke, and Michael I. Bonne. Effects of Mixed Mode I/II Loading and Grain Orientation on Crack Initiation and Stable Tearing in 2024-T3 Aluminum. *Fatigue and Fracture Mechanics*, 27:105–125, 1997.
- Y. Anderberg. Modelling Steel Behaviour. *Fire Safety Journal*, 13(1):17–26, APR 7 1988.
- T. L. Anderson. *Fracture Mechanics : Fundamentals and Applications*. Boca Raton, FL : CRC Press, c2005., 2005. ISBN 0849316561.
- Dengqi Bai, Laurie Collins, Fathi Hamad, Xiande Chen, Randy Klein, and Joe Zhou. X100 (Grade 690) Helical-Welded Linepipe. In *Proceedings of the 7th International Pipeline Conference*, Calgary, Alberta, Canada, 2014.
- G.I. Barenblatt. The formation of equilibrium cracks during brittle fracture: General ideas and hypothesis, axially symmetric cracks. *Journal of Applied Mathematics and Mechanics*, 23(3):622–636, 1959.

- G.I. Barenblatt. The mathematical theory of equilibrium cracks in brittle fracture. *Advan. Appl. Mech.*, 7:55–129, 1962.
- Zdeněk P. Bažant and M. T. Kazemi. Determination of fracture energy, process zone length and brittleness number from size effect, with application to rock and concrete. *International Journal of Fracture*, 44:111–131, 1990. ISSN 0376-9429.
- R. Becker, a. Needleman, O. Richmond, and V. Tvergaard. Void growth and failure in notched bars. *Journal of the Mechanics and Physics of Solids*, 36(3):317–351, 1988.
- L. Benabou, Z. Sun, and P.R. Dahoo. A thermo-mechanical cohesive zone model for solder joint lifetime prediction. *International Journal of Fatigue*, 49:18 – 30, 2013. ISSN 0142-1123.
- T Børvik, O.S Hopperstad, T Berstad, and M Langseth. A computational model of viscoplasticity and ductile damage for impact and penetration. *European Journal of Mechanics - A/Solids*, 20(5):685–712, 2001.
- S. J. Burns and Z. J. Bilek. The Dependence of the Fracture Toughness of Mild Steel on Temperature and Crack Velocity. *Metallurgical Transactions*, 4:975–984, 1973.
- J Capelle, J Furtado, Z Azari, S Jallais, and G Pluvinage. Design based on ductile – brittle transition temperature for API 5L X65 steel used for dense CO₂ transport. *Engineering Fracture Mechanics*, 110:270–280, 2013. ISSN 0013-7944.
- J. Capelle, M. Ben Amara, G. Pluvinage, and Z. Azari. Role of constraint on the shift of ductile-brittle transition temperature of subsize Charpy specimens. *Fatigue & Fracture of Engineering Materials & Structures*, 37(12):1367–1376, 2014. ISSN 8756758X.

- Cheng Cen. *Characterization and calculation of fracture toughness for high grade pipes*. PhD thesis, University of Alberta, 2012.
- Sourayon Chanda and C Q Ru. FEA modeling of dynamic fracture of pipeline steel at low temperatures. In *9th European Solid Mechanics Conference*, Leganés-Madrid, Spain, 2015a.
- Sourayon Chanda and CQ Ru. Cohesive zone model for temperature dependent fracture analysis of pipeline steel. In *Proceedings of 25th Canadian Congress on Applied Mechanics*, number 1, pages 1–4, London, Ontario, Canada, 2015b.
- Y. J. Chao, J. D. Ward, and R. G. Sands. Charpy impact energy, fracture toughness and ductile-brittle transition temperature of dual-phase 590 Steel. *Materials and Design*, 28(2):551–557, 2007. ISSN 02641275.
- Ju Chen, Ben Young, and Brian Uy. Behavior of High Strength Structural Steel at Elevated Temperatures. *Journal of Structural Engineering*, 132(12):1948–1954, 2006. ISSN 0733-9445.
- Arild H. Clausen, Tore Børvik, Odd S. Hopperstad, and Ahmed Benallal. Flow and fracture characteristics of aluminium alloy AA5083–H116 as function of strain rate, temperature and triaxiality. *Materials Science and Engineering: A*, 364(1-2):260–272, 2004.
- Alfred Cornec, Ingo Scheider, and Karl Heinz Schwalbe. On the practical application of the cohesive model. *Engineering Fracture Mechanics*, 70(14):1963–1987, 2003.
- A. Coseru, J. Capelle, and G Pluvinage. On the use of Charpy Transition Temperature as reference temperature for the choice of a pipe steel. In *5th International Conference on Computational Mechanics and Virtual Engineering*, number October, pages 1–10, Brasov, Romania, 2013.

- F. Costanzo and D.H. Allen. A continuum mechanics approach to some problems in subcritical crack propagation. *International Journal of Fracture*, 63(1):27–57, 1993.
- D.S. Dugdale. Yielding of steel sheets containing slits. *Journal of the Mechanics and Physics of Solids*, 8(2):100–104, 1960. ISSN 00225096.
- F Ebrahimi and H. K. Seo. Ductile crack initiation. *Acta Metallurgica*, 44(2):831–843, 1996.
- M. Elices, G.V. Guinea, J. Gómez, and J. Planas. The cohesive zone model: advantages, limitations and challenges. *Engineering Fracture Mechanics*, 69(2):137–163, 2002. ISSN 00137944.
- H. A. Elliott. An analysis of the conditions for rupture due to griffith cracks. *Proceedings of the Physical Society*, 59(2):208–223, 1947.
- M. Fagerström and R. Larsson. A thermo-mechanical cohesive zone formulation for ductile fracture. *Journal of the Mechanics and Physics of Solids*, 56(10):3037–3058, 2008.
- P. Fassina, F. Bolzoni, G. Fumagalli, L. Lazzari, L. Vergani, and a. Sciuccati. Influence of hydrogen and low temperature on pipeline steels mechanical behaviour. *Procedia Engineering*, 10:3226–3234, 2011.
- H. G. Hillenbrand G. Demofonti, G. Mannucci and D. Harris. Suitability evaluation of X100 steel pipes for high pressure gas transportation pipelines by full scale tests. *2004 International Pipeline Conference*, pages 1685–1692, 2004.
- Luca Gambirasio and Egidio Rizzi. On the calibration strategies of the Johnson–Cook strength model: Discussion and applications to experimental data. *Materials Science and Engineering: A*, 610:370–413, 2014.

Leonardo Barbosa Godefroid, Luiz Cláudio Cândido, Rodrigo Vicente, and Bayão Toffolo. Microstructure and Mechanical Properties of Two Api Steels for Iron Ore Pipelines 2 . Materials and Experimental Procedures. *Materials Research*, 2014.

A. L. Gurson. Continuum Theory of Ductile Rupture by Void Nucleation and Growth: Part I—Yield Criteria and Flow Rules for Porous Ductile Media. *Journal of Engineering Materials and Technology*, 99(1):2, 1977.

Seung Youb Han, Sang Yong Shin, Sunghak Lee, Nack J. Kim, Jin-Ho Bae, and Kisoo Kim. Effects of Cooling Conditions on Tensile and Charpy Impact Properties of API X80 Linepipe Steels. *Metallurgical and Materials Transactions A*, 41(2):329–340, December 2009. ISSN 1073-5623.

T J Holmquist and G R Johnson. Determination of constants and comparison of results for various constitutive models. *Journal de Physique III*, 1(C3):853–860, 1991.

Qing Yu Hou and Jing Tao Wang. A modified Johnson–Cook constitutive model for Mg–Gd–Y alloy extended to a wide range of temperatures. *Computational Materials Science*, 50(1):147–152, November 2010. ISSN 09270256.

GR Johnson and WH Cook. A constitutive model and data for metals subjected to large strains, high strain rates and high temperatures. In *Proceedings of the 7th International Symposium on Ballistics*, pages 541–547, The Hague, Netherlands, 1983.

GR Johnson and WH Cook. Fracture characteristics of three metals subjected to various strains, strain rates, temperatures and pressures. *Engineering fracture mechanics*, 21(I), 1985.

Dae-Ho Jung, Jae-Ki Kwon, Nam-Sub Woo, Young-Ju Kim, Masahiro Goto, and Sangshik Kim. S–N Fatigue and Fatigue Crack Propagation Behaviors of X80 Steel at

- Room and Low Temperatures. *Metallurgical and Materials Transactions A*, 45(2): 654–662, October 2013.
- L. M. Kachanov. Rupture time under creep conditions. *Problems of Continuum Mechanics*, pages 202–218, 1961.
- M. Kachanov. On the Concept of Damage in Creep and in the Brittle-Elastic Range. *International Journal of Damage Mechanics*, 3(4):329–337, 1994. ISSN 1056-7895.
- A. A. Kaminskii and G. V. Galatenko. On the Temperature Dependence of Fracture Toughness in the Brittle-to-Ductile Transition Region. *International Applied Mechanics*, 35(4):80–86, 1999.
- MF Kanninen, EF Rybicki, RB Stonesifer, D Broek, AR Rosenfield, and GT Nalin. Elastic–plastic fracture mechanics for two-dimensional stable crack growth and instability problems. *ASTM STP 668*, pages 121–150, 1979.
- H Kobayashi and H Onoue. Brittle Fracture of Liberty Ships. Technical Report March, Oregon State, USA, 1943.
- Heikki Kotilainen. Determination of the cleavage fracture stress and the temperature dependence of the fracture toughness of Cr-Mo-V steel. Technical report, Metals Laboratory, Report 41, Technical Research Centre of Finland, 1979.
- Poh-Sang Lam, Yil Kim, and Yuh J Chao. Crack tip opening displacement and angle for a growing crack in carbon steel. In *2005 ASME Pressure Vessels and Piping Division Conference*, pages 1–8, Denver, Colorado, USA, 2005.
- Jean Lemaitre. A Continuous Damage Mechanics Model for Ductile Fracture. *Journal of Engineering Materials and Technology*, 107:83–89, 1985.

- Jing Ma, Xiaoyong Zhang, Shixia Cheng, and Huilin Gao. Influence of Partitioning Process on the Microstructure and Mechanical Properties of High Deformability Oil-Gas Pipeline. *Advances in Mechanical Engineering*, pages 1–11, 2014.
- E. Marotta, M. Minotti, and P. Salvini. Effect of fracture tunneling in DWT Tests. *Engineering Fracture Mechanics*, 81:33–42, 2012. ISSN 00137944.
- M A Meyers, Y Chen, F D S Marquis, and D S Kim. High-Strain , High-Strain-Rate Behavior of Tantalum. 26:2493–2501, 1995.
- M. Minotti and P. Salvini. Deep fracture profile effect on DWT test for pipeline characterization. In *6th Pipeline Technology Conference*, 2011.
- Srdjan Nešić. Key issues related to modelling of internal corrosion of oil and gas pipelines - A review. *Corrosion Science*, 49(12):4308–4338, 2007.
- J. C. Newman. An elastic–plastic finite element analysis of crack initiation, stable crack growth, and instability. *ASTM STP 833*, page 93–117, 1984.
- J. C. Newman, M. A. James, and U. Zerbst. A review of the CTOA/CTOD fracture criterion. *Engineering Fracture Mechanics*, 70(3-4):371–385, 2003.
- Kyoungsoo Park and Glaudio H. Paulino. Cohesive Zone Models : A Critical Review of Traction-Separation Relationships Across Fracture Surfaces. *Applied Mechanics Reviews*, 64(November 2011):20, 2013. ISSN 0003-6900.
- Shreya Parmar. *Simulation of Ductile Fracture in Pipeline Steels under Varying Constraint Conditions Affairs*. PhD thesis, Carleton University, Ottawa, Ontario, 2014.
- Alejandro G. Perez-Bergquist, Yanwen Zhang, Tamas Varga, Sandra Moll, Fereydoon Namavar, and William J. Weber. Temperature-dependent void formation and growth

- at ion-irradiated nanocrystalline CeO₂-Si interfaces. *Nuclear Instruments and Methods in Physics Research, Section B: Beam Interactions with Materials and Atoms*, 325:66–72, 2014.
- Zhang Qingdong, Cao Qiang, and Zhang Xiaofeng. A Modified Johnson-Cook Model for Advanced High-Strength Steels Over a Wide Range of Temperatures. *Journal of Materials Engineering and Performance*, 23(12):4336–4341, 2014. ISSN 1059-9495.
- B. W. Qiu. *Research on Ductile Fracture of X80 Pipeline Steel and Finite Element Simulation*. [in chinese], Wuhan University of Science and Technology, Wuhan, China, 2010.
- Y.N. Rabotnov. *Creep Problems in Structural Members*. Applied Mathematics and Mechanics Series. Elsevier, 1969. ISBN 9780444102591.
- Z.J. Ren and C.Q. Ru. Numerical investigation of speed dependent dynamic fracture toughness of line pipe steels. *Engineering Fracture Mechanics*, 99:214–222, February 2013.
- J.R. Rice and D.M. Tracey. On the ductile enlargement of voids in triaxial stress fields. *Journal of the Mechanics and Physics of Solids*, 17(3):201–217, 1969.
- JA Rinebolt and WJ Harris. Effect of alloying elements on notch toughness of pearlitic steels. *Transactions of the American Society for Metals*, 43:1175–1214, 1951.
- D.L Rudland, G.M Wilkowski, Z Feng, Y.-Y Wang, D Horsley, and A Glover. Experimental investigation of CTOA in linepipe steels. *Engineering Fracture Mechanics*, 70(3-4):567–577, 2003. ISSN 00137944.
- William K. Rule and S.E. Jones. A Revised Form for the Johnson–Cook Strength Model. *International Journal of Impact Engineering*, 21(8):609–624, 1998.

- Ingo Scheider, Aida Nonn, Alexander Völling, A. Mondry, and Christoph Kalwa. A Damage Mechanics based Evaluation of Dynamic Fracture Resistance in Gas Pipelines. *Procedia Materials Science*, 3(July 2015):1956–1964, 2014.
- Chang-Sung Seok. Effect of Temperature on the Fracture Toughness of A516 Gr70 Steel. *KSME International Journal*, 14:11–18, 2000.
- Do-Jun Shim, Gery Wilkowski, Da-Ming Duan, and Joe Zhou. Effect of Fracture Speed on Ductile Fracture Resistance - Part 1: Experimental. In *Proceedings of the 8th International Pipeline Conference*, number 127 mm, Calgary, Alberta, Canada, 2010.
- F. Shimizu, S. Ogata, and J. Li. Theory of shear banding in metallic glasses and molecular dynamics calculations. *Materials Transactions*, 48(11):2923–2927, 2007.
- Sang Yong Shin, Byoungchul Hwang, Sangho Kim, and Sunghak Lee. Fracture toughness analysis in transition temperature region of API X70 pipeline steels. *Materials Science and Engineering A*, 429(1-2):196–204, 2006.
- W A Sorem, R H Dodds, and S T Rolfe. Effects of crack depth on elastic plastic fracture toughness. *Int. J. Fracture*, 47(2):105–126, 1991.
- C.T. Sun and Z.-H. Jin. Cohesive zone model-chapter 9. In C.T. SunZ.-H. Jin, editor, *Fracture Mechanics*, pages 227 – 246. Academic Press, Boston, 2012. ISBN 978-0-12-385001-0.
- Dávid Széplaky, Zsolt Vaszi, and Augustin Varga. Effect of Temperature Distribution Around Pipelines for Transportation of Natural Gas on Environment. 3:33–40, 2013.
- Yoshio Terada, Mitsugu Yamashita, Takuya Hara, Hiroshi Tamehiro, and Naoshi Ayukawa. Development of API X100 UOE line pipe, 1997. ISSN 0300306X.

Shunsuke Toyoda, Sota Goto, Takatoshi Okabe, Hideto Kimura, Satoshi Igi, Yutaka Matsui, Satoru Yabumoto, Akio Sato, Masahito Suzuki, and Tomohiro Inoue. Metallurgical Design and Performance of ERW Linepipe With High-Quality Weld Seam Suitable for Extra-Low-Temperature Services. In *Volume 3: Materials and Joining*, volume 3, page 439. ASME, 2012.

V. Tvergaard and a. Needleman. Analysis of the cup-cone fracture in a round tensile bar. *Acta Metallurgica*, 32(1):157–169, 1984.

K. Y. Volokh. Comparison between cohesive zone models. *Communications in Numerical Methods in Engineering*, 20(11):845–856, 2004.

Sheng-hui Wang, Yonggang Zhang, and Weixing Chen. Room temperature creep and strain-rate-dependent stress-strain behavior fo pipeline steels. *Journal of Materials Science*, 36:1931–1938, 2001.

Yang Wang, Yuanxin Zhou, and Yuanming Xia. A constitutive description of tensile behavior for brass over a wide range of strain rates. *Materials Science and Engineering: A*, 372(1-2):186–190, May 2004. ISSN 09215093.

G Wilkowski, D Rudland, DJ Shim, FW Brust, and Sudarsanam Babu. Advanced Integration of Multi-scale Mechanics and Welding Process Simulation in Weld Integrity Assessment. Technical Report June, Engineering Mechanics Corporation of Columbus, Columbus, Ohio, 2008.

William D. Callister. *Fundamentals of Material Science and Engineering*. John Wiley & Sons, Inc., 5th edition, 2001.

Youyou Wu, Hailiang Yu, Cheng Lu, Kiet Tieu, Ajit Godbole, and Guillaume Michal. Transition of ductile and brittle fracture during DWTT by FEM. In *13th International Conference on Fracture*, pages 1–8, Beijing, China, 2013.

J Xu, Z L Zhang, E Ø stby, B Nyhus, and D B Sun. Effects of Temperature and Crack Tip Constraint on Cleavage Fracture Toughness in the Weld Thermal Simulated X80 Pipeline Steels. In *Proceedings of the 20th International Offshore and Polar Engineering Conference*, volume 7, pages 163–169, Beijing, China, 2010.

P.S. Yu and C.Q. Ru. Strain rate effects on dynamic fracture of pipeline steels: Finite element simulation. *International Journal of Pressure Vessels and Piping*, 126-127: 1–7, February 2015. ISSN 03080161.

H. Yuan and W. Brocks. On the J-integral concept for elastic-plastic crack extension. *Nuclear Engineering and Design*, 131(2):157–173, 1991.

X-K Zhu, Bn Leis, and Sw Dean. Constraint Corrected J-R- Curve and Its Application to Fracture Assessment for X80 Pipelines. *Journal of ASTM International*, 3(6): 13209, 2006.